the plant journal

SEB SOCIETY FOR EXPERIMENTAL BIOLOGY

The Plant Journal (2026) **125,** e70644 doi: 10.1111/tpj.70644

Regulatory network rewiring drives strain-specific lipid accumulation response in *Chlorella sorokiniana* under nutrient starvation

Claudio C. Barrera-Duarte, Ricardo A. Chávez Montes[†], Héctor-Rogelio Nájera-González and Damar Lopez-Arredondo[*]
Department of Plant and Soil Science, Institute of Genomics for Crop Abiotic Stress Tolerance, Texas Tech University, Lubbock 79409, Texas, USA

Received 4 July 2025; revised 2 November 2025; accepted 1 December 2025.
*For correspondence (e-mail damar.lopez-arredondo@ttu.edu).
[†]Present address: Department of Biology, Indiana University, Bloomington, Indiana 47405, USA

SUMMARY

Microalgae modulate lipid metabolism in response to nutrient stress, offering a promising avenue for sustainable biofuel production. However, a mechanistic understanding of the transcriptional programs driving triacylglycerol (TAG) accumulation remains limited, particularly in non-model species. Here, we employ a systems-level approach to dissect the regulatory basis of TAG biosynthesis in two *Chlorella sorokiniana* strains exhibiting contrasting lipid accumulation phenotypes under nitrogen (—N) and phosphorus (—P) deprivation. Through physiological, metabolic, and transcriptomic analyses, we confirmed *C. sorokiniana* DOE1412 (*Cs*DOE1412) as a high TAG-accumulator and *C. sorokiniana* UTEX1228 (*Cs*1228) as a low TAG-accumulator, providing a comparative framework for inferring transcriptional regulatory networks (TRNs). Both stressors induced rapid TAG accumulation within 6 h, with *Cs*DOE1412 reaching 40% TAG content by 48 h under —N conditions. While N deprivation primarily promoted TAG accumulation, P starvation favored diacylglyceryl trimethylhomoserine biosynthesis, reaching up to 21 and 30% of the lipid composition in *Cs*1228 and *Cs*DOE1412, respectively. TRNs analysis revealed a distinct regulatory logic between strains: *Cs*DOE1412 exhibited a stress-specific, narrowly focused transcriptional response, with five transcription factors (TFs) identified as leading regulators based on centrality measures, whereas *Cs*1228 mounted a broader, overlapping response, with 30 key TFs across conditions. A detailed analysis of the inferred TRNs identified 15 and 14 candidate TFs in *Cs*DOE1412 and *Cs*1228, respectively, with predicted interactions involving key steps in carbon metabolism and lipid biosynthesis, suggesting their involvement in metabolic rewiring during nutrient stress. Among them, we found two CH3-type ortholog pairs, *Cs1228_21g10473*/*CsDOE1412_2079g07848* and *Cs1228_02g00899*/*CsDOE1412_2296g01133*, showing upregulation in TAG-accumulating conditions; and one AP2-type ortholog pair, *Cs1228_04g03113*/*CsDOE1412_2160g02163*, with contrasting transcription profiles, pointing to transcriptional regulatory pathways with shared and unique regulators between strains. These findings expand the repertoire of regulatory components associated with algal lipid metabolism and highlight *C. sorokiniana* as a robust model for elucidating complex transcriptional responses to environmental cues. Furthermore, this study provides candidate TFs for engineering enhanced lipid productivity in microalgae.

Keywords: *Chlorella sorokiniana*, nitrogen starvation, phosphorus starvation, triacylglycerol accumulation, transcriptional regulatory networks, transcription factors.

INTRODUCTION

Abiotic stresses have been widely applied to stimulate the accumulation of neutral storage lipids in microalgae to pursue sustainable biofuel feedstocks (Sajjadi et al., 2018). Among the most common stressors, nitrogen deprivation (—N) induces triacylglycerol (TAG) accumulation in a variety of microalgal species, including *Chlamydomonas reinhardtii*, *Chlorella sorokiniana*, *Chlorella vulgaris*, *Nannochloropsis gaditana*, and *Nannochloropsis oceanica* (Hu et al., 2008; Song et al., 2022). In these systems, nutrient stress not only promotes TAG deposition in lipid bodies (LBs), which may contribute to mitigating photooxidative damage (Ischebeck et al., 2020), but also triggers profound

metabolic remodeling characterized by chloroplast degradation, membrane lipid turnover, and starch accumulation (Kong et al., 2018; Mathiot et al., 2019; Vijayan et al., 2024). Such conditions frequently impair growth and biomass accumulation, hindering the efforts to achieve the dual objectives of maximizing lipid yield and cell productivity for scalable applications.

Strategies to enhance lipid production have largely focused on manipulating genes encoding rate-limiting enzymes in Carbon metabolism and TAG biosynthetic pathways (Mulgund, 2022). These include acyl-CoA diacylglycerol acyltransferase (La Russa et al., 2012), acyltransferases (Deng et al., 2012), lipases, phospholipase (Trentacoste et al., 2013), fatty acid (FA) desaturases (Peng et al., 2014; Zäuner et al., 2012), thioesterase (Radakovits et al., 2011), and malate dehydrogenase (Xue et al., 2015), whose activities vary in response to different stress conditions. While the genetic manipulation of metabolic genes has provided some mechanistic insights, their success in enhancing lipid accumulation while maintaining optimal growth has been limited, highlighting the need for higher-order regulatory targets.

An emerging and promising approach involves the modulation of transcriptional regulators to coordinate multiple nodes within lipid biosynthesis and primary metabolism. Although this strategy offers a more integrative and potentially effective approach, its application in microalgae remains relatively underdeveloped. Some transcription factors (TFs), including compromised hydrolysis of triacylglycerols 7 (CHT7), nitrogen response regulator 1 (NRR1), R2R3-type MYB family (MYB1), rhythm of chloroplast 40 (ROC40), and phosphate starvation response 1 (PSR1), have been implicated in regulating TAG biosynthesis in *C. reinhardtii* under nutrient deprivation (Bajhaiya et al., 2016; Boyle et al., 2012; Choi et al., 2022; Goncalves et al., 2016; Tsai et al., 2014). Nevertheless, the underlying transcription regulatory networks (TRNs) orchestrating lipid accumulation under environmental stress remain poorly characterized, even in this model system, and are largely unknown in non-model strains with robust TAG production potential.

A systems-level approach to inferring and analyzing gene regulatory networks (GRNs) offers an integrative view of lipid metabolic regulation under stress and holds promise for identifying conserved lineage-specific TFs that orchestrate TAG accumulation (Gargouri et al., 2015). Such analyses may enable the discovery of core regulatory modules and inform rational engineering strategies to decouple lipid biosynthesis from growth penalties. While *C. reinhardtii* continues to serve as a valuable genetic model, its relatively low biomass yield and cell density restrict its utility for biotechnological applications (Fields et al., 2018). In contrast, *C. sorokiniana* stands out as a high-performing microalga with broad bioenergy and biotechnological potential (Neofotis et al., 2016). Some *C. sorokiniana* strains accumulate lipids up to 25% of their dry cell weight (DCW) under standard conditions, and this can increase to 50% DCW upon —N (Adams et al., 2013). In comparison, phosphorus deficiency (—P) is generally less effective in inducing lipid accumulation. *Chlorella sorokiniana* also exhibits faster growth rates, the ability to produce a wide range of secondary metabolites, and an excellent lipid profile comparable to that of soybean oil, the dominant biodiesel source in the U.S. (Del Campo et al., 2003; Pelah et al., 2004; Shi & Chen, 2002; Wang & Chen, 2008).

Chlorella strains display wide growth and lipid accumulation responses to nutrient starvation (Maltsev et al., 2023; Zhu et al., 2015). A comparative analysis of five *Chlorella* species, *C. sorokiniana*, *C. vulgaris*, *Chlorella emersonii*, *Chlorella minutissima*, and *Chlorella protothecoides*, highlighted marked differences in growth inhibition and lipid productivity under —N conditions (Illman et al., 2000). For instance, the growth of *C. vulgaris*, *C. sorokiniana*, and *C. emersonii* was significantly inhibited, whereas *C. minutissima*, and *C. protothecoides* were less affected. TAG content increased by 122, 177, and 108% in *C. vulgaris*, *C. emersonii*, and *C. protothecoides*, respectively, while *C. sorokiniana* showed only a 10% increase (Illman et al., 2000). Other studies report lipid contents as high as 222% for *C. sorokiniana* and 377% for *C. vulgaris* (Adams et al., 2013; Breuer et al., 2013; Fan et al., 2014; Liang et al., 2009; Wan et al., 2011), suggesting that culture conditions can significantly impact TAG accumulation. These findings underscore the complexity of the regulatory mechanisms governing microalgal responses to nutrient stress and their linkage to lipid biosynthesis. Understanding these unique phenotypic/genotypic properties will facilitate the development of genetic engineering strategies for strain improvement.

In this study, we leverage the physiological and genetic plasticity of *C. sorokiniana* to investigate the transcriptional regulation that governs TAG accumulation under nutritional stress. We performed comparative physiological, metabolic, and transcriptional studies of two *C. sorokiniana* strains, named *C. sorokiniana* DOE1412 (hereafter *Cs*DOE1412) and *C. sorokiniana* UTEX 1228 (hereafter *Cs*1228), exposed to —N and —P conditions. *Cs*DOE1412 was characterized as a high TAG-accumulator, whereas *Cs*1228 exhibited a low TAG phenotype. Using TRNs inference, we uncovered candidate TFs with putative regulatory interactions with rate-limiting steps in the carbon and lipid metabolism, implicating them in stress-responsive metabolic rewiring. These findings advance our understanding of nutrient stress-mediated lipid regulation in microalgae and establish *C. sorokiniana* as a tractable system for dissecting complex transcriptional circuits underlying lipid metabolic plasticity.

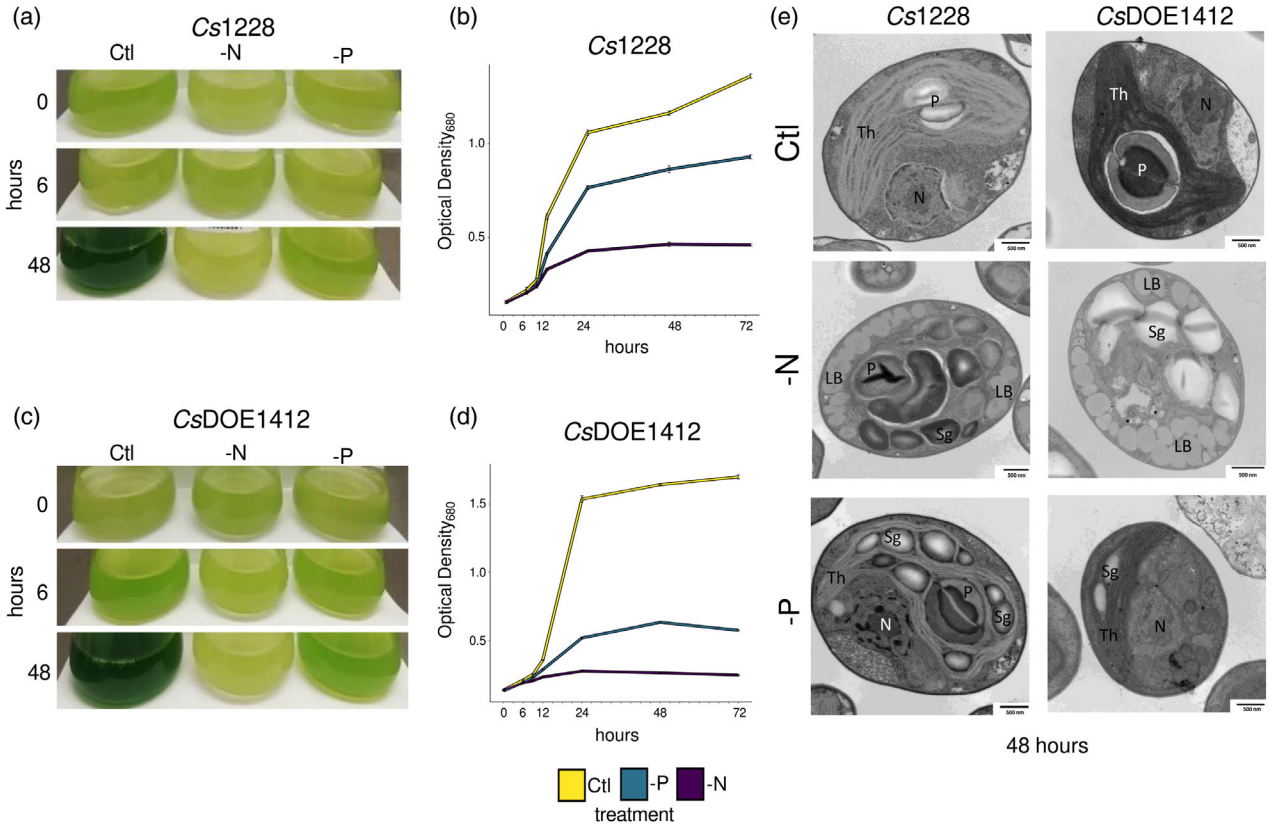

Figure 1. Effects of nitrogen and phosphorus starvation on the growth and lipid accumulation of *Chlorella sorokiniana* strains.
Chlorella sorokiniana UTEX1228 (*Cs*1228) (a) and *C. sorokiniana* DOE1412 (*Cs*DOE1412) (c) were cultivated under control (Ctl), phosphorus starvation (—P), and nitrogen starvation (—N) conditions. Representative photographs of the cultures at 15 min, 6 h, and 48 h of stress are shown.
(b, d) Culture growth of both strains was measured as optical density at 680 nm (OD_{680}) at different timepoints (0, 6, 12, 24, 48, and 72 h).
(e) *Cs*1228 and *Cs*DOE1412 cells were harvested after 48 h of growth under control and nutrient stress conditions, fixed, and prepared for imaging using transmission electron microscopy. LB, lipid bodies; N, nucleus; P, pyrenoid; Sg, starch granules; Th, thylakoids.

RESULTS

P and N starvation reduce the growth of *Cs*1228 and *Cs*DOE1412, while inducing lipid remodeling and TAG accumulation

We first performed time-course experiments to assess how —N and —P affect growth and TAG accumulation in *C. sorokiniana* strains *Cs*DOE1412 and *Cs*1228. The growth of nutrient-starved and control algae cultures (complete tris acetate phosphate [TAP] media) was followed for 72 h. Both stresses significantly reduced growth in both strains, with a more severe impact in *Cs*DOE1412 (Figure 1a–d). In —P, growth was reduced by 32% in *Cs*1228 and 67% in *Cs*DOE1412; under —N, reductions were 67 and 86%, respectively (Figure 1a–d). After 48 h of stress, the cultures were pale green and less dense, indicating chlorophyll loss. Correspondingly, chlorophyll content decreased significantly under —N in both strains but remained unchanged under —P (Figure S1). Transmission electron microscopy (TEM) revealed severe thylakoid disorganization and damage under —N, while —P-stressed cells retained relatively intact chloroplast ultrastructure (Figure 1e). We also observed a more significant accumulation of LBs at 48-h post-stress in *Cs*DOE1412 compared to *Cs*1228, consistent with elevated TAG accumulation, while *Cs*1228 accumulated more starch granules than *Cs*DOE1412 in both —N and —P conditions (Figure 1e). These observations support a distinct physiological impact of —N and —P on carbon accumulation and the photosynthetic machinery in each strain.

Ion chromatography (IC) was used to determine the rate of N (NH_4^+) and P (PO_4^{-3}) consumption of both *C. sorokiniana* strains grown under control conditions. N levels decreased from 116 to 61.4 ppm in *Cs*1228 and 68.8 ppm in *Cs*DOE1412 within 6-h post-inoculation, and further declined to approximately 55 ppm in both cultures after 48 h, indicating similar rates of N uptake. In contrast, P dynamics differed between strains. *Cs*DOE1412 showed an important reduction to from 27 to 22.7 ppm at 6 h, whereas *Cs*1228 exhibited delayed P uptake, with lower P levels observed only after 48 h. *Cs*DOE1412 maintained relatively stable P concentrations at the same timepoint

(Data S1), suggesting distinct P uptake kinetics between the two strains.

To investigate lipid remodeling under stress, we profiled lipid composition using ultra-high performance liquid chromatography coupled to mass spectrometry (UHPLC–MS) at 6- and 48-h post-stress. The lipidomic datasets included 3237 and 2790 compounds in *Cs*1228 and *Cs*DOE1412, respectively (Data S2). Major lipid classes detected included TAG, phosphatidylcholine (PC), phosphatidylethanolamine (PE), galactolipids [mono (MGDG) and digalactosyldiacylglycerol (DGDG)], and betaine lipids [diacylglycerol-trimethyl homoserine (DGTS)], and were expressed in terms of total lipid content (Figure 2).

Under control conditions, TAGs abundance was low at 6 h (7% in *Cs*1228, 5% in *Cs*DOE1412) and significantly decreased at 48 h. PE, PC, MGDG, and DGDG remained relatively stable over time in both strains and collectively comprised 46 (*Cs*1228) and 63% (*Cs*DOE1412) of the total lipid content (Figure 2; Figure S2). N starvation induced sustained TAGs accumulation in both strains at both timepoints, reaching 24 and 40% of the total lipid content in *Cs*1228 and *Cs*DOE1412, respectively, after 48 h (Figure 2; Figure S2). In contrast, —P stress triggered moderate TAG accumulation at 6 h (13% in *Cs*1228, 25% in *Cs*DOE1412), but levels declined by 48 h, coinciding with a marked increase in DGTS (21% in *Cs*1228, 30% in *Cs*DOE1412) and a decrease in PC (Figure 2; Figure S2). Under control and —N conditions, DGTS represented less than 0.5% of total lipids, suggesting a —P-specific response.

P and N starvations elicit different FA compositions of TAG

TAGs produced by *Cs*DOE1412 exhibited greater FA diversity and complexity compared to *Cs*1228 (Figure S3). In both strains, TAGs primarily contained long-chain FAs with 16 and 18 carbon atoms, but *Cs*DOE1412 uniquely synthesized TAGs incorporating very long-chain FAs (up to C22–C24). Nutrient starvation elicited the synthesis of distinct TAG species in each strain. At 6 h of —N and —P, *Cs*DOE1412 predominantly accumulated 16:0_16:3_18:3, 16:0_18:2_18:2, 16:0_18:1_18:2, 16:0_16:0_16:3, and 16:0_16:0_16:2, while *Cs*1228 was enriched in 16:0_16:3_18:3, 16:0_17:1_17:1, 16:0_16:2_18:2, 16:0_18:2_22:0, and 16:0_16:3_18:3 (Figure S3). These TAGs accumulated further over the course of N starvation but remained low or undetectable under —P by 48 h. Notably, *Cs*DOE1412 synthesized a broader set of —N exclusive, polyunsaturated FAs (PUFAs)-rich TAG species, such as 18:2_18:3_18:3, 18:2_18:2_20:0, and 16:2_16:3_18:3, that were absent in *Cs*1228 and not detected in response to —P (Figure S3).

To obtain a more comprehensive TAG profiling, FA methyl esters (FAMEs) were analyzed by gas chromatography–mass spectrometry (GC–MS) in control and stressed samples at 6 and 48 h. Among the 36 components in the FAME standard mix, five were identified across samples, indicating the presence of saturated FAs (SFAs), monounsaturated FAs (MUFAs), and PUFAs in varying proportions (Table 1; Table S1). Key FAMEs included methyl palmitate (C16:0), methyl oleate (C18:1), methyl linoleate (C18:2), methyl linolenate (C18:3), methyl stearate (C8:0), and methyl hexanoate (C6:0), the latter detected only in *Cs*DOE1412 (Table S1). *Cs*DOE1412 accumulated significantly higher total FAMEs under all conditions than *Cs*1228 (Table 1). Under —N, FAMEs content in *Cs*DOE1412 increased from 273.05 $\mu g\ g^{-1}$ dry weight (DW) at 6 h to 419.47 $\mu g\ g^{-1}$ DW at 48 h, whereas *Cs*1228 produced only 56.27 and 64.34 $\mu g\ g^{-1}$ DW at the same timepoints (Table 1). A similar trend was observed in —P, although with lower FAMEs amounts; *Cs*DOE1412 increased from 222.6 $\mu g\ g^{-1}$ DW at 6 h to 241.15 $\mu g\ g^{-1}$ DW at 48 h, whereas *Cs*1228 produced only 42.9 and 50 $\mu g\ g^{-1}$ DW at the corresponding timepoints (Table 1).

Biofuel profiles predominantly composed of SFAs and MUFAs, which determine oxidation resistance and liquidity at low temperatures, have been associated with biofuels with enhanced functional properties for commercial applications (Hawrot-Paw et al., 2021; Levasseur et al., 2020). Likewise, low levels of PUFAs have been shown to have positive effects on biodiesel flow properties. SFAs and MUFAs together were found to be the major FAME components across nutrient stress treatments and timepoints in the two strains, ranging from 46 to 71%, although *Cs*1228 showed a lower potential for total FAME accumulation than *Cs*DOE1412 (Table 1). *Cs*DOE1412 showed a higher proportion of PUFAs compared to *Cs*1228 in response to both stresses, although the values were, in general, lower than those in control conditions. These data highlight *Cs*DOE1412's superior lipid productivity and its potential for biofuel applications and further study of the transcriptional regulation of lipid accumulation in response to nutrient stress.

P and N starvation elicit differential transcriptional responses in *Cs*1228 and *Cs*DOE1412

To dissect the molecular mechanisms underlying the distinct physiological and metabolic responses of *Cs*1228 and *Cs*DOE1412 to —N and —P, we performed a comparative RNA-seq analysis. Three timepoints were selected to capture both early and sustained transcriptional changes: 15 min (t1), 6 h (t2), and 48 h (t3) post-transfer to stress conditions (see Materials and Methods).

Uniform manifold approximation and projection (UMAP) revealed strain- and stress-specific transcriptional dynamics. *Cs*1228 exhibited a rapid transcriptional shift under —N, with a distinct profile already detectable at t1. In contrast, its response to —P became more apparent at t2 and t3. *Cs*DOE1412 displayed no changes at t1 but a clear separation from controls at t2 and t3 (Figure 3a). The

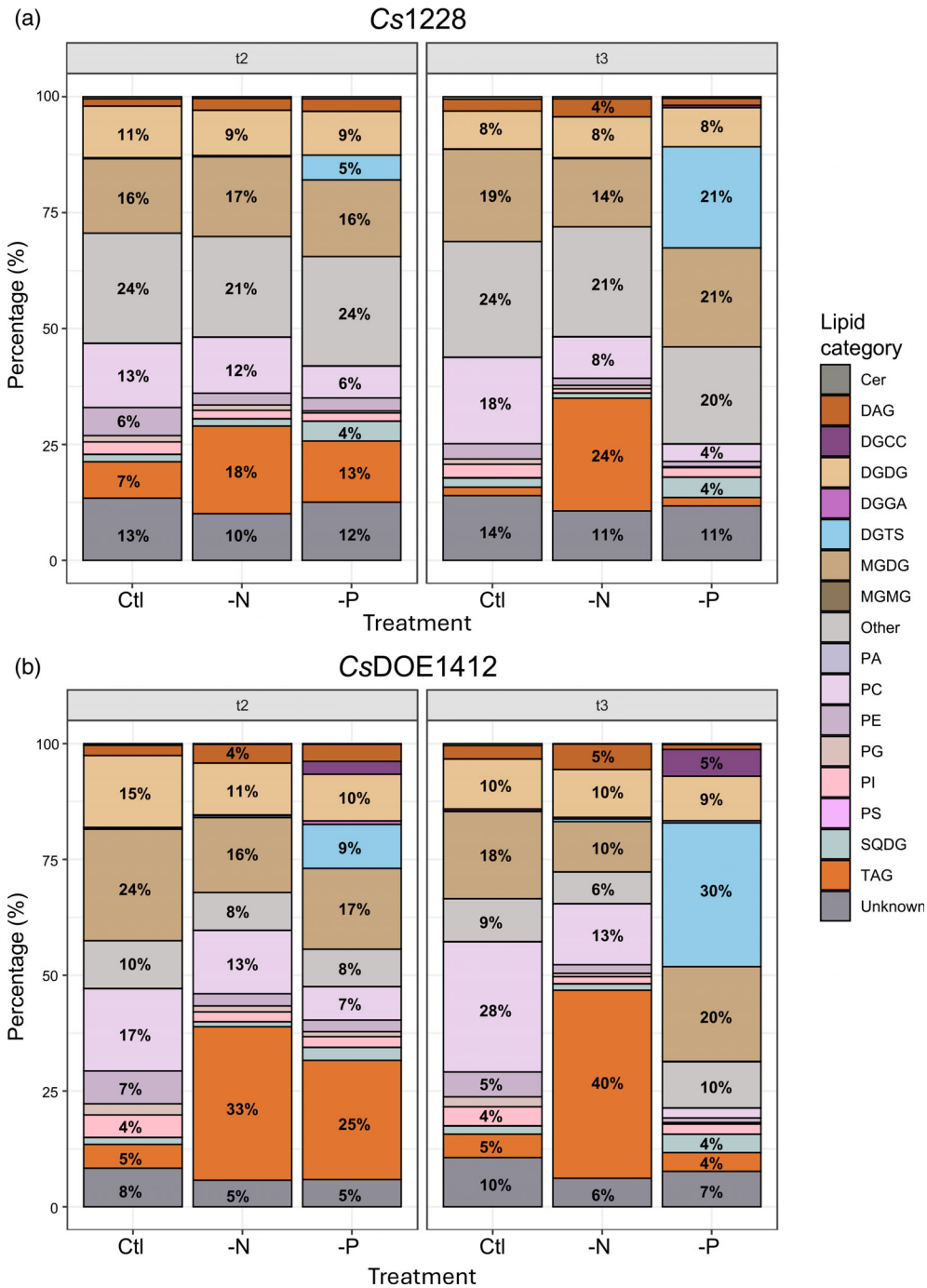

Figure 2. Relative abundance of major lipid categories in *Chlorella sorokiniana* strains grown under phosphorus or nitrogen starvation for 6 (t2) and 48 h (t3). (a) *Chlorella sorokiniana* UTEX1228 (*Cs*1228) and (b) *C. sorokiniana* DOE1412 (*Cs*DOE1412) were cultivated under Control (Ctl), phosphorus starvation (—P), and nitrogen starvation (—N) conditions, and biomass was used to determine major lipid categories by UHPLC–MS at 6 (t2) and 48 (t3) h after inoculation, with six replicates per treatment per strain. The graphs represent the total lipid content for each condition and each area represents the abundance of the corresponding lipid category relative to the total lipid content, expressed as a percentage. Cer, ceramide; DAG, diacylglycerol; DGCC, diacylglyceryl-3-O-carboxyhydroxymethylcholine; DGDG, digalactosyldiacylglycerol; DGGA, diacylglyceryl glucuronide; DGTS, diacylglyceryl trimethylhomoserine; MGDG, monogalactosyldiacylglycerol; MGMG, monogalactosylmonoacylglycerol; PA, phosphatidic acid; PC, phosphatidylcholine; PE, phosphatidylethanolamine; PG, phosphatidylglycerol; PI, phosphatidylinositol; PS, phosphatidylserine; SQDG, sulfoquinovosyl diacylglycerol; TAG, triacylglycerol; Other, lipids identified by name different to the previous categories; Unknown, lipids identified by molecular formula only.

Table 1 Grouping of fatty acid methyl ester (FAME) content (μg g^{-1} dry biomass)[a] according to the number of double bonds in the hydrocarbon chain in *Cs*1228 and *Cs*DOE1412 cultured in medium with sufficient nitrogen and phosphorus (Ctl), without nitrogen (—N), or without phosphorus (—P) for 6 h (t2) and 48 h (t3)

	t1			t3		
FAME group	Ctl	—P	—N	Ctl	—P	—N
*Cs*1228						
SFAs (C16:0; C18:0)	53.10 (60%)	23.62 (55%)	27.5 (49%)	36.37 (50%)	26.34 (53%)	32.19 (50%)
MUFAs (C18:1)	4.5 (5%)	2.85 (7%)	12.37 (22%)	3.32 (5%)	2.98 (6%)	10.82 (17%)
PUFAs (C18:2c; C18:3c)	31.36 (35%)	16.43 (38%)	16.4 (29%)	33.16 (45%)	20.68 (41%)	21.33 (33%)
Total per treatment (μg g^{-1} dry biomass,[a] 100%)	88.96	42.9	56.27	72.85	50	64.34
*Cs*DOE1412						
SFAs (C6:0; C16:0; C18:0)	113.1 (44%)	106.83 (48%)	135.49 (50%)	92.47 (38%)	104.2 (43%)	186.65 (44%)
MUFAs (C18:1)	9.01 (4%)	14.65 (7%)	30.46 (11%)	2.31 (1%)	7.51 (3%)	42.59 (11%)
PUFAs (C18:2c; C18:3c)	134.1 (52%)	101.18 (45%)	107.1 (39%)	145.45 (61%)	129.44 (54%)	187.65 (44%)
Total per treatment (μg g^{-1} dry biomass,[a] 100%)	256.51	222.66	273.05	240.23	241.15	419.47

Note: Percentage of each group relative to the total of all groups per treatment is indicated in parentheses. The designation of fatty acids groups is given in accordance with the IUPAC guidelines.
Abbreviations: MUFAs, monounsaturated fatty acids; PUFAs, polyunsaturated fatty acids; SFAs, saturated fatty acids.
[a]Values are the sum of the participating FAMEs in each group.

magnitude of the transcriptional response varied markedly between strains, with an overall trend of transcriptional downregulation under both stresses at the late timepoint in *Cs*DOE1412 (Figure 3b,c). Under —N, *Cs*1228 displayed a robust and sustained response with 2519 downregulated and 2392 upregulated differentially expressed genes (DEGs) at t1, increasing to 3090 downregulated and 3374 upregulated DEGs at t2, and 2685 downregulated and 2456 upregulated DEGs at t3 (Figure 3b; Data S3). Under —P, transcriptional responses in *Cs*1228 were evident at t2 and t3, with 1559 downregulated and 2373 upregulated DEGs at t2, and 1706 downregulated and 1792 upregulated DEGs at t3. No DEGs were found at t1 under —P. In contrast, *Cs*DOE1412 showed a more discrete transcriptional response. No DEGs were detected at t1 under either stress. Under —N, 219 DEGs were downregulated and 368 upregulated at t2, with 796 downregulated DEGs and 513 upregulated DEGs at t3. Under —P, 108 downregulated and 101 upregulated DEGs at t2, and 612 downregulated and 528 upregulated DEGs at t3 (Figure 3c; Data S3). Upset plots revealed time- and treatment-specific DEGs and genes shared across timepoints and stress conditions, highlighting complex regulatory networks (Figure S4a–d; Data S4). The transcriptional landscape of both strains under control conditions also changed over time, highlighting a similar trend.

Gene ontology (GO) category enrichment analysis showed common and strain-specific cellular mechanisms in responses to N and P starvation

GO category enrichment analysis showed that cells of both strains deployed cellular responses to —N, N reutilization, and C reallocation since their earliest timepoint. Accordingly, within the top 25 enriched GO categories in upregulated DEGs we found 'GO:0006995 cellular response to nitrogen starvation', 'GO:0006541 glutamine metabolic process', and 'GO:0006526 arginine biosynthetic process' shared in both strains (Figure 3d,e). Within these categories, specific genes coding for high-affinity N transporters, N regulatory P-II-like protein, and enzymes related to arginine, glutamate, and urea metabolism, such as arginosuccinate synthase, arginyltransferase, arginosuccinase, glutamine synthetase, glutamine amidotransferase, were found (Data S5).

GO terms enriched in response to —P varied between strains (Figure S5a,b). For instance, 'GO:0016036 cellular response to phosphate starvation' term was enriched at t2 and t3 in *Cs*DOE1412 only (Figure S5B), along with mechanisms related to P transport and scavenging ('GO:0006817 phosphate ion transport' and 'GO:0046434 organophosphate metabolic process'). Genes encoding H^+/Pi

Figure 3. Phosphorus and nitrogen starvation induce differential transcriptional responses in *Chlorella sorokiniana* strains. RNA-sequencing analysis was performed for both *C. sorokiniana* strains, C. *sorokiniana* UTEX1228 (*Cs*1228) and *C. sorokiniana* DOE1412 (*Cs*DOE1412), grown under Control (Ctl), phosphorus starvation (—P), and nitrogen starvation (—N) conditions 15 min (t1), 6 h (t2), and 48 h (t3) after inoculation.
(a) UMAP plot shows the dimensional reduction analysis and clustering of RNA-seq libraries generated in this study. Each shape (triangle, circle) represents one replicate, and colors denote treatment and timepoint.
(b, c) show the number of differentially expressed genes (DEGs), up- (green) and downregulated (magenta), determined for both strains under different experimental conditions.
(d, e) The plots show the most significantly enriched Gene Ontology categories in the upregulated DEGs in response to nutrient stress conditions for both strains in (b, c). Differential expression in response to the stress was calculated relative to the corresponding control conditions at the same timepoint.

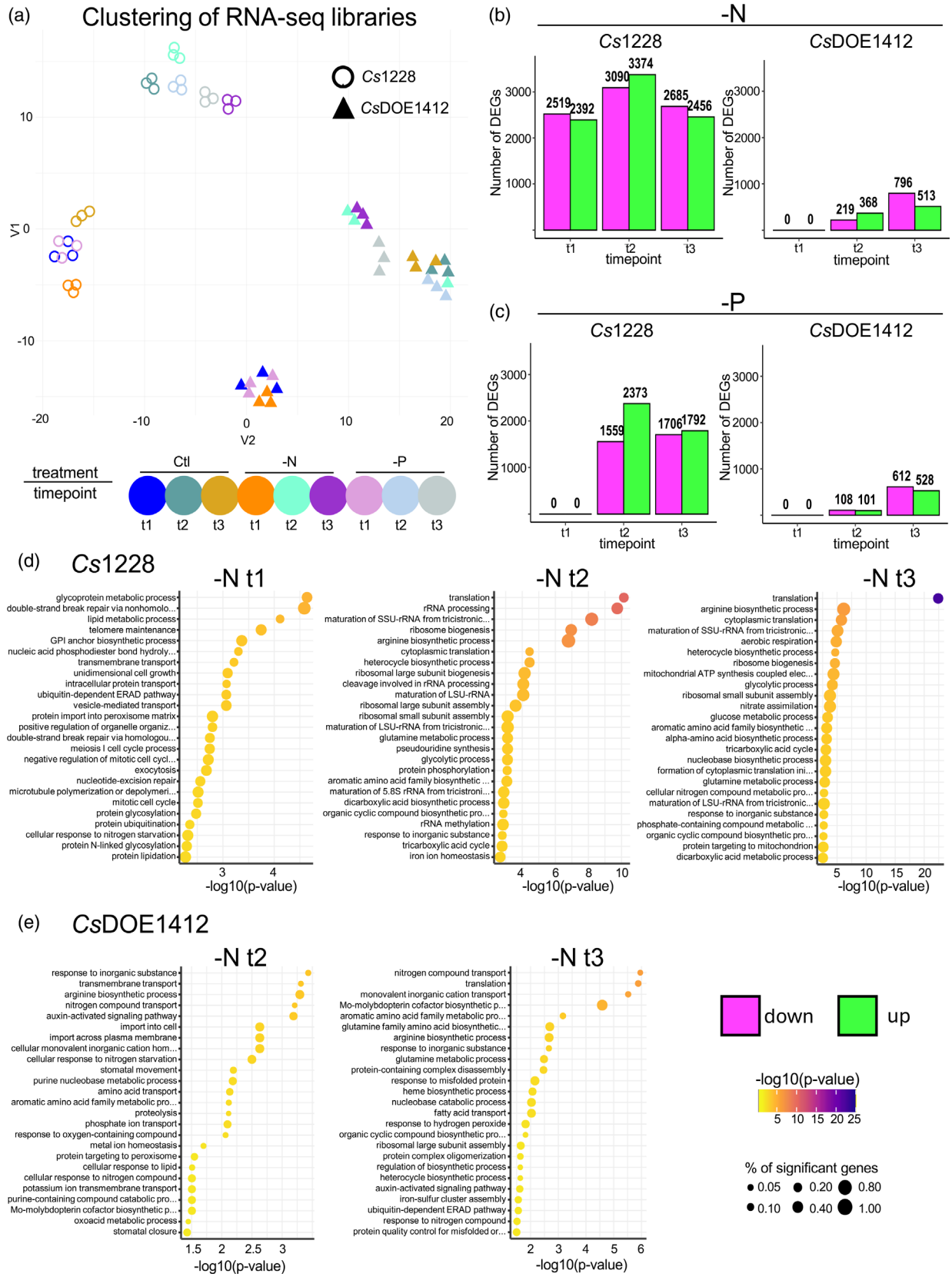

cotransporters, phosphate transporters, and a SPX-domain containing protein belonged to these categories (Data S5). In contrast, in *Cs*1228 under —P treatment enriched GO terms were involved in various stress-related processes, such as the response to reactive oxygen species ('GO:0098869 cellular oxidant detoxification' and 'GO:0006749 glutathione metabolic process'), and secondary metabolism ('GO:0019748 secondary metabolic process', 'GO:0009698 phenylpropanoid metabolic process', 'GO:0006664 glycolipid metabolic process') (Figure S5a). Nevertheless, we found categories, such as 'GO:0016311 dephosphorylation' and 'GO:0015698 inorganic anion transport' under the same stress condition, which included genes coding for various phosphatases and phosphate transporters, likely pointing to the scavenging and mobilization of phosphate in *Cs*1228 (Data S5).

GO categories related to global C metabolism and lipid metabolism were also enriched in upregulated DEGs in *Cs*1228 and *Cs*DOE1412 under both stresses. 'GO:0006629 lipid metabolic process', 'GO:0071396 cellular response to lipid', 'GO:0016042 lipid catabolic process', and 'GO:0006650 glycerophospholipid metabolic process', 'GO:0006099 tricarboxylic acid cycle', among others, were mainly enriched under —N t1, —N t2, and —N t3 in both strains, and —P t2 in *Cs*1228 (Figure S5a,b). These categories include several genes related to broad lipid metabolism, like the ortholog genes encoding for glycerol-3-phosphate acyltransferase (GPAT), a key enzyme in TAG biosynthesis, and citrate synthase, which catalyzes a key enzymatic step in the TCA and glyoxylate cycle (Fukuda et al., 2018; Theodoulou & Eastmond, 2012) (Figure 3; Data S5). In —P t3, enriched GO categories included 'GO:0009247 glycolipid biosynthetic process', 'GO:0019252 starch biosynthetic process,' 'GO:0006650 glycerophospholipid metabolic process' in both *Cs*1228 and *Cs*DOE1412, with no related GO categories enriched at t2 in *Cs*DOE1412.

The top 25 GO categories of downregulated DEGs under —N at the different timepoints in both strains were enriched in crucial processes such as nucleic acid metabolism, photosynthesis, and cell division. Those included for instance, 'GO:0009765 photosynthesis and light harvesting', 'GO:0015995 chlorophyll biosynthetic process', 'GO:0009767 photosynthesis electron transport chain', 'GO:0010207 photosystem II assembly', 'GO:0009658 chloroplast organization', 'GO:0051301 cell division', and 'GO:0006260 DNA replication', suggesting an adverse effect of N deficiency on overall cell growth and functioning (Figure S6). Similar GO categories, except those related to photosynthesis, were enriched in the downregulated DEGs under —P (Figure S7), which correlated with a greener culture in both strains (Figure 1; Figure S1). However, enriched GO categories related to photosynthesis were present in the Top50 in *Cs*1228 under —P (Figure S7).

Distinct sets of TFs are differentially expressed in *Cs*1228 and *Cs*DOE1412 in response to N and P starvation

Transcriptional responses to external inputs entail complex, fine-tuned, and dynamic interactions between transcription regulators, resulting in downstream cellular processes that enable organisms to cope with an ever-changing environment. These transcriptional responses are controlled by TFs, the primary regulators of gene expression, and other molecular mediators, such as chromatin remodelers, that form a network that governs gene expression (Aoki et al., 2007). We used the Plant Transcription Factor Database (PlantTFDB) (Jin et al., 2017) to identify TFs potentially involved in establishing the transcriptional responses to nutrient stresses in both *Chlorella* strains. As we observed important transcriptional changes in the control samples (no nutrient stress) as time progressed (Figure S8) and to enrich robustness in the transcriptional responses, comparisons between each starvation timepoint versus the earliest timepoint in nutrient-sufficient conditions were made, for example, —N t2 versus Ctl t1, —N t3 versus Ctl t1, —P t2 versus Ctl t1. This new dataset included the suffix 'V2' (Data S3) and was found to increase the number of DEGs for each comparison compared to the original contrast (Figure S8). We identified 163 and 75 unique differentially expressed TFs (across at least one starvation treatment and timepoint) in *Cs*1228 and *Cs*DOE1412, respectively (Figure S9a,b). Differentially expressed TFs in *Cs*1228 belong to 28 different families, whereas those in *Cs*DOE1412 belong to 18 (Figure S10a,b). Around 40% of the responsive TFs for all treatments and timepoints were members of only three TF families in each strain: SBP, GATA, and C3H in *Cs*1228, and MYB-related, SBP, and C3H in *Cs*DOE1412 (Figure S10a,b). This suggests that a few TF families primarily drive transcriptional responses to nutrient stress.

An upset analysis helped us determine the sets of shared and unique differentially expressed TFs between the different timepoints of —N and —P per strain (Figure 4a–d). Notably, TFs downregulated exclusively at —P t2 were the most numerous intersections in both strains. Most of the remaining intersections were contrasting between strains. For instance, the intersection of upregulated TFs shared across all conditions includes 18 TFs in *Cs*1228 and only one in *Cs*DOE1412 (Figure 4a,c). Similarly, there were 17 downregulated TFs in the intersection between all treatments in *Cs*1228 and zero in *Cs*DOE1412 (Figure 4b,d).

Each starvation treatment and timepoint had a distinct TF transcriptional profile, and the expression patterns of these TFs across the treatments and timepoints were diverse (Figure S9a,b). While some TFs maintained their up- or downregulation across conditions, others showed a fluctuating up-to-downregulation, or vice versa, suggesting that they play crucial roles in establishing and progressing

the transcriptional responses in both strains (Figure S9a,b). To explore further the expression trends of the TFs, we calculated the *z*-scores of all TFs across samples (185 for *Cs*1228 and 200 for *Cs*DOE1412) and performed hierarchical clustering to determine if they grouped into clusters. All TFs were found to group into five clusters (Figure 4e,f; Data S6), and all showed expression peaks for both strains, with a general negative expression trend at t2 across all treatments. Clusters 2 and 4 showed contrasting trends in both strains at the same timepoints and stress conditions. Cluster 3 in *Cs*1228 shows a preponderant role under —N t2, remaining unchanged under —P.

TRNs unveil major TFs potentially controlling responses to N and P starvations in *Cs*1228 and *Cs*DOE1412

To uncover the transcriptional regulatory interactions involved in the responses to —N and —P in *Cs*1228 and *Cs*DOE1412, the calculated expression matrix in transcripts per million (TPM) from RNA-seq libraries was fed to the Algorithm for the Reconstruction of Accurate Cellular Networks (ARACNe) to generate the TFs interaction network (TFsNet) and the TF-non-TF network (TF-non-TFNet) separately (Table S2) (Margolin, Nemenman, et al., 2006; Margolin, Wang, et al., 2006). Both types of networks were merged to generate the full network of TFs and their interactors per strain, which were termed FullNet_*Cs*1228 and FullNet_*Cs*DOE1412 (Table S2). The FullNet obtained at DPI 0.0 contained 11 022 nodes and 35 274 edges in the case of *Cs*1228 and 10 825 nodes and 28 920 edges in the case of *Cs*DOE1412 (Data S7). These TRNs represent each strain's potential transcriptional regulatory interactions. Due to their high degree of modularity, TRNs can help us determine whether TFs and TF-controlled genes with similar transcriptional profiles belong to the same gene community (grouped in the network) and conserve the same transcriptional interactions across treatments. To gain insights into the TRN's biological significance, the minimum spanning tree subgraph was calculated, and relevant modules (gene communities or graph clustering) were retrieved using the Louvain algorithm (mst-net) (Table S2) (Blondel et al., 2008). Gene communities were enriched in common and strain-specific biological processes in the two strains (Figure S11a,b). Among the common gene communities, arginine biosynthesis/N transport, autophagy, membrane transport, and DNA replication and repair were found. Specific gene communities included lipid metabolism and FA metabolism in *Cs*DOE412 (Figure S11b), whereas photosynthesis, circadian rhythm, chloroplast, and chlorophyll biosynthesis were found in *Cs*1228 (Figure S11a). These data showed a degree of correlation with the nutrient stress responses of both strains.

The FullNet_*Cs*1228, FullNet_*Cs*DOE1412, and the lists of DEGs were then used to generate the subnetworks of DEGs and TFs (Figures S12 and S13) for each strain, starvation treatment, and timepoint, termed DEGs_Subnet (Table S2). The inferred subnetworks showed a dramatic change in the transcriptional landscape of both strains as the nutrient starvations progressed from t1 to t3 (Figures S12 and S13). As both strains showed different transcriptional interactions between TFs and non-TFs interactors for each DEGs_Subnet, we applied the robust rank aggregation (RRA) algorithm to integrate the most influential nodes based on five network centrality measures (degree, closeness, betweenness, eigenvector, and PageRank). We assigned significance scores according to the method (Kolde et al., 2012). Thirty and five TFs were found as leading transcriptional regulators of cell responses to both —N and —P in *Cs*1228 and *Cs*DOE1412, respectively (with a cutoff of *P*-value <0.05) (Figure 5a,b). These TFs were referred to as RRA top-ranked TFs. We then identified the first interactors of these TFs in each DEGs_Subnet and evaluated how the interactions shifted over time in response to —N and —P. For both strains, we identified unique and shared interactions (Figure 5c,d). Interestingly, *Cs*1228 had more common interactors regulated in response to both stresses throughout time than *Cs*DOE1412. In *Cs*1228, 46.1 and 68.7% of interactors were found at the inner intersection of the Venn diagrams in —N and —P, respectively, whereas only 12.9 and 10.7% were shared in *Cs*DOE1412 for the same stress conditions (Figure 5c,d). This points to different transcriptional programs regulating responses to —N and —P in the two strains, with *Cs*1228 deploying a broader and shared set of TFs and interactors responding to nutrient stress. Conversely, *Cs*DOE1412 responds with a more restricted and unique transcriptional program to every condition. A GO categories enrichment analysis of the interactors in these intersections showed that in *Cs*DOE1412, biological processes related to vesicle biogenesis and trafficking ('GO:0006890', 'GO:0006891'), photosynthesis ('GO:0015979'), and cell division ('GO:0051301'), regulation of biosynthetic process ('GO:0009889'), and translation ('GO:0006412') are enriched. In contrast, in *Cs*1228, processes related to RNA metabolism and translation are more enriched ('GO:0006364', 'GO:0006418', 'GO:0001732', 'GO:0006412') (Figure S14; Data S8). This suggests that the regulation of cell division, photosynthesis, and LB formation and homeostasis underlies the *Cs*DOE1412 high-lipid accumulation phenotype.

We investigated whether regulatory nodes and their interactions are conserved between both strains. Orthogroups were generated based on sequence homology among nodes, and then, transcriptional regulatory interactions conserved between *Cs*1228 and *Cs*DOE1412 for each treatment and timepoint, that is, t2 and t3, were identified in the corresponding subnetworks and termed Ortho_Subnet (Table S2; Data S9). In the case of —N conditions, we found subnetworks of conserved regulatory interactions at t2 and t3 between both strains. A GO

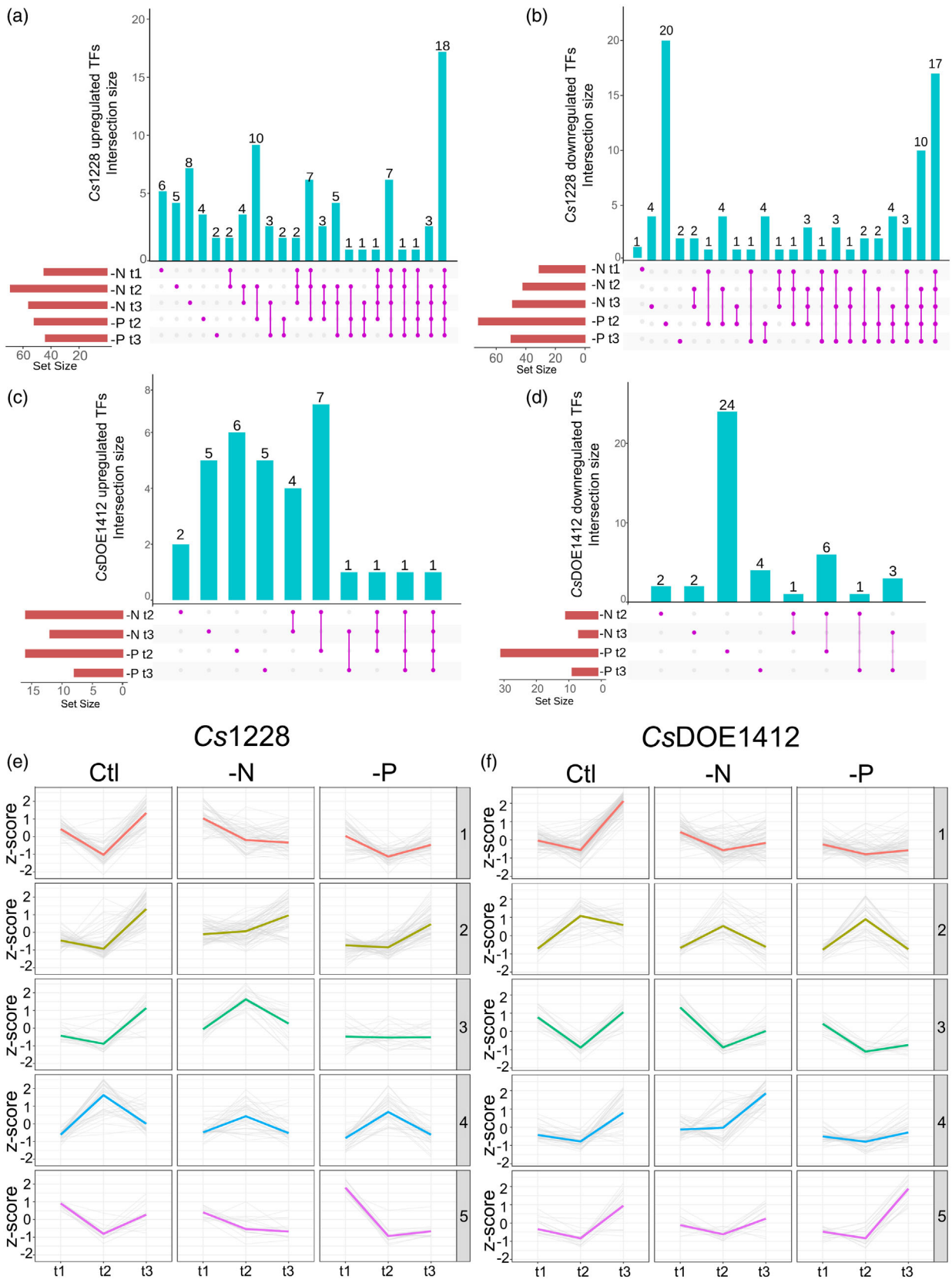

Figure 4. Transcription factors (TFs) show diverse expression patterns in response to phosphorus and nitrogen starvation in *Chlorella sorokiniana* strains. Upset analysis of differentially expressed TFs in response to nitrogen starvation (—N) and phosphorus starvation (—P) in (a, b) *C. sorokiniana* UTEX1228 (*Cs*1228) and (c, d) *C. sorokiniana* DOE1412 (*Cs*DOE1412) at 15 min (t1), 6 h (t2), and 48 h (t3) after inoculation. The analysis was performed for up- and downregulated TFs separately. Differentially expressed genes unique to each condition and shared between two or more conditions are represented with pink dots and connections, and the number is noted above each cyan bar. Intersections with zero genes were not included in the plots. Differentially expressed TFs in (e) *Cs*1228 and (f) *Cs*DOE1412 were clustered into five groups by their *z*-score using Ward's method. Trend lines are based on each cluster's mean of scaled values. Cluster number is indicated at the right end of the corresponding panels.

enrichment analysis showed DNA replication and cell cycle ('GO:0006270 DNA replication initiation', 'GO:0000278 mitotic cell cycle', 'GO:0051301 cell division, and others') among the most enriched GO categories in the Ortho_Subnet_Nt2 (Figure S15). In contrast, specific N starvation response and N metabolism categories ('GO:0071705 nitrogen compound transport', 'GO:0042128 nitrate assimilation', and 'GO:0043562 cellular response to nitrogen levels') are enriched in the Ortho_Subnet_Nt3 (Figure S15). These results suggest a strong connection between cell division and —N responses, as observed in culture growth and transcriptome analysis in both strains. In the case of —P condition, a conserved subnetwork enriched in DNA metabolism and cell division GO categories (e.g., GO:0006270 DNA replication initiation, GO:0051301 cell division) was identified at t2 (Figure S15), whereas no enriched GO categories were found at t3. Overall, these data suggest that in the case of —N responses, core transcriptional circuits are conserved between strains, leading to cellular responses with similar trends, and that the TRNs of the —P response had strongly diverged between both strains as time progressed. However, the superior TAG accumulation and fewer RRA top-ranked TFs in *Cs*DOE1412 may reflect tighter transcriptional regulation, allowing it to reprogram cellular metabolism more effectively toward lipid storage.

Identification of TFs regulating TAG accumulation and rate-limiting steps of global carbon metabolism

To identify specific TFs that regulate TAG accumulation in both strains, genes encoding the enzymatic steps of pathways directly influencing TAG accumulation, namely FA biosynthesis, TAG biosynthesis, TAG degradation, starch biosynthesis, and starch degradation, were retrieved from each strain's global enzyme-coding gene repertoire. Then, their inferred transcriptional regulators in the FullNet_*Cs*1228 and FullNet_*Cs*DOE1412 were identified (see Materials and Methods). We identified 75 and 44 TFs that potentially control different enzymatic steps of these pathways in *Cs*1228 and *Cs*DOE1412, respectively (Figure S16). At first glance, the differential expression of these sets of TFs across treatments suggested that positive and negative transcriptional regulators are involved in TAG accumulation. Therefore, we rationalized different scenarios for these TFs to participate in TAG accumulation: They can be up or downregulated at the three TAG accumulation conditions (—N t2, —N t3, and —P t2) regardless of the nutrient stress or show differential responses to the stress and time (up or down in —N t2 and —N t3, up or down in —N t2 and —P t2), but should not be differentially expressed at —P t3, when both strains had very low TAG content and the microalgae cells shifted to DGTS accumulation. We found that 14 (three downregulated and 11 upregulated) and 15 (five downregulated and 10 upregulated) TFs were differentially expressed in *Cs*1288 and *Cs*DOE1412, respectively, under high TAG accumulation conditions (Figure 5e). These TFs were referred to as TAG-related *TFs* (Table S2). Three TAG-related TFs, two members of the C3H family and one from the AP2 family, have orthologs in both *Chlorella* strains. The two pairs of C3H orthologs, Cs1228_21g10473/CsDOE1412_2079g07848 and Cs1228_02g00899/CsDOE1412_2296g01133, were upregulated in both species under all conditions. The AP2 orthologs, however, had contrasting differential expression profiles; *Cs1228_04g03113* was upregulated in —N t2 and —P t2, and *CsDOE1412_2160g02163* was downregulated in —N t2, —N t3, and —P t2 (Figure 5e).

To investigate how these TAG-related TFs potentially control global metabolic changes associated with carbon metabolism, 13 rate-limiting steps of the central carbon partition pathways were selected (see Materials and Methods), which showed variable expression patterns (Figure 6). The selected enzymatic steps and associated pathways are: (1) 6-phosphofructokinase (PFK)/glycolysis; (2) RuBisCO/Calvin Cycle; (3) isocitrate dehydrogenase (IDH)/TCA cycle; (4) citrate synthase and (5) malate synthase/glyoxylate cycle; (6) glucose-1-phosphate adenylyltransferase (ADPGase)/starch biosynthesis; (7) acetyl-CoA carboxylase (ACCase)/FA biosynthesis; (8) GPAT, and (9) diacylglycerol O-acyltransferase (DGAT)/*de novo* TAG biosynthesis; (10) phospholipid: diacylglycerol acyltransferase (PDAT) and (11) galactolipase (PGD1), alternative acyl donor enzymatic steps for TAG production; (12) betaine lipid synthase 1 (BTA1)/DGTS biosynthesis; and (13) major lipid droplet protein (MLDP)/lipid droplet membrane formation. From the 13 rate-limiting steps, eight were inferred to be controlled by TAG-related TFs in each strain (enzymatic steps 1, 2, 5, 6, 7, 8, 9, and 10). In comparison, four (enzymatic steps 3, 4, 12, and 13) were inferred to be controlled by TAG-related TFs only in *Cs*1228, and one enzymatic step (11) did not show any

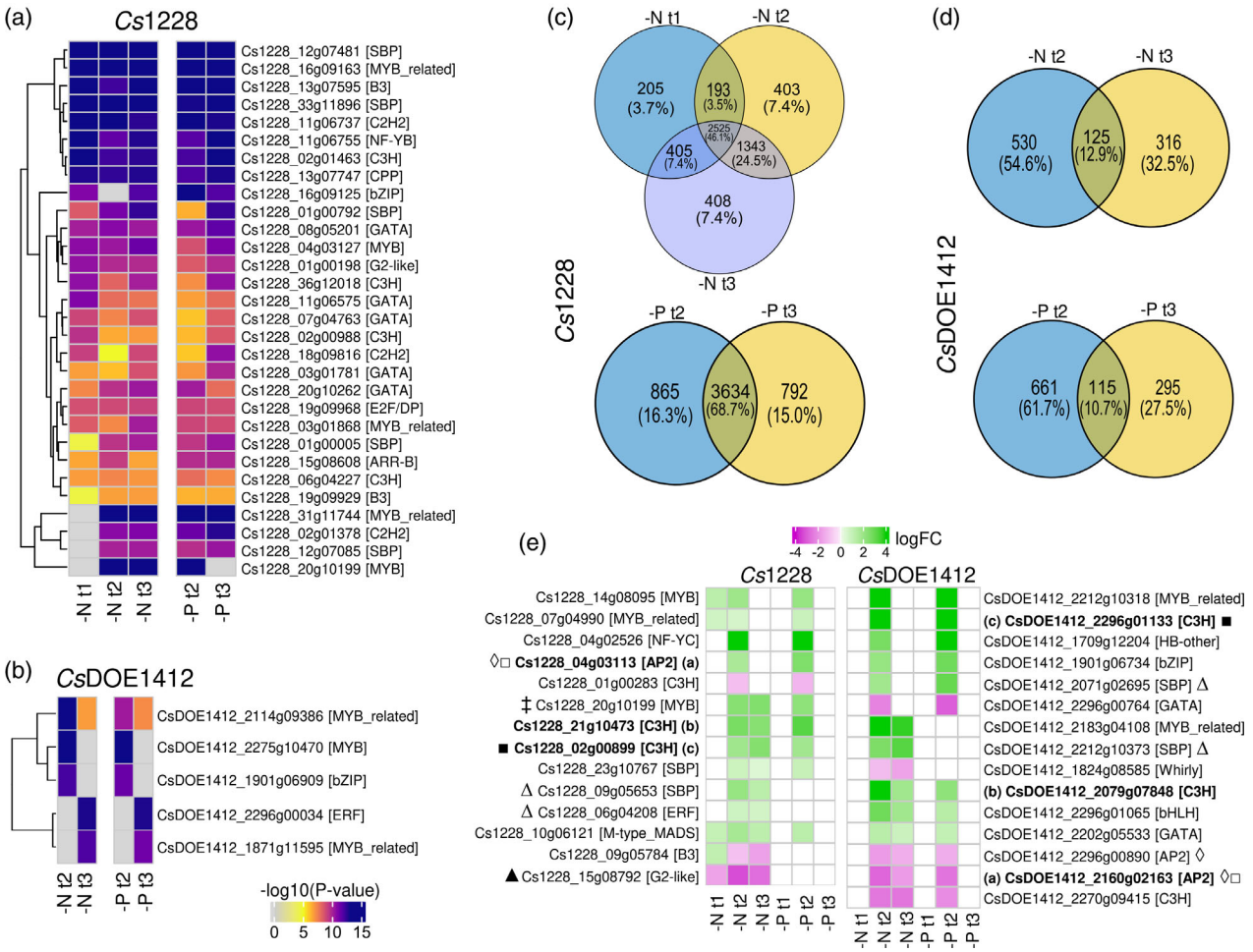

Figure 5. Transcription factors (TFs) controlling the most significant regulatory nodes in *Chlorella sorokiniana* strains in response to phosphorus and nitrogen starvation.

Subnetworks of differentially expressed genes (DEGs) and TFs were generated for both *C. sorokiniana* UTEX1228 (*Cs*1228) and *C. sorokiniana* DOE1412 (*Cs*DOE1412) in response to nitrogen starvation (—N) and phosphorus starvation (—P) at 15 min (t1), 6 h (t2), and 48 h (t3) after inoculation. These networks were termed DEGs_Subnet. The robust rank aggregation (RRA) algorithm was used to identify the most significant nodes across the DEGs_Subnet(s) in (a) *Cs*1228 and (b) *Cs*DOE1412. The heatmaps show RRA significance score of the top-ranked nodes (TFs) in the DEGs_Subnet for each strain under different experimental conditions. The TF family is shown in brackets. First-level interactors of TFs in (a) and (b) were identified. The Venn diagrams show the sets of interactors that are unique or shared among stress conditions and timepoints for (c) *Cs*1228 and (d) *Cs*DOE1412.

(e) An analysis was conducted to identify differentially expressed TFs under different experimental conditions, which control genes encoding for the enzymatic steps of pathways that directly influence TAG accumulation. These TFs were termed 'TAG-related TFs'. The heatmap shows the expression pattern of the 14 and 15 TFs identified in *Cs*1228 and *Cs*DOE1412, respectively. Colorkey represents the gene expression logFC value for each TF under stress at different timepoints relative to the control condition at t1. The TF family is shown in brackets. TFs labeled with letters (a), (b), and (c) indicate orthology between the corresponding pair of genes in *Cs*1228 and *Cs*DOE1412. Symbols in the other genes indicate homology found in other organisms, such as *Chlamydomonas reinhardtii* NRR1 (Δ) and PSR1 (▲); *Auxenochlorella protothecoides* ApMYB6 (‡); *Glycine max* GmZF351, GmZF392 (■) and GmWRI1 (□); and *Arabidopsis thaliana* AtWRI1 (◊).

Figure 6. Differential expression of *Chlorella sorokiniana* genes encoding enzymes catalyzing rate-limiting steps in the global lipid metabolism.

Rate-limiting steps in the global lipid metabolism were identified from the literature, and the ortholog genes in *C. sorokiniana* UTEX1228 (*Cs*1228) and *C. sorokiniana* DOE1412 (*Cs*DOE1412) were retrieved (see Materials and Methods). Sign Significance (ssign) of differential expression, in response to nitrogen starvation (—N) and phosphorus starvation (—P) at 15 min (t1), 6 h (t2), and 48 h (t3) after inoculation, is shown as heatmaps for every predicted gene. Numbers in pink circles indicate the enzymatic steps as in Figure 7: (1) 6-phosphofructokinase (PFK, EC 2.7.1.11)/glycolysis; (2) RuBisCO (EC 4.1.1.39)/Calvin Cycle; (3) Isocitrate dehydrogenase (IDH, EC 1.1.1.41)/TCA cycle; (4) citrate synthase (EC 2.3.3.1), and (5) malate synthase (EC 2.3.3.9)/glyoxylate cycle; (6) Glucose-1-phosphate adenylyltransferase (ADPGase, EC 2.7.7.27)/starch biosynthesis; (7) acetyl-CoA carboxylase (ACCase, EC 6.4.1.2)/FA biosynthesis; (8) glycerol-3-phosphate O-acyltransferase (GPAT, EC 2.3.1.15) and (9) diacylglycerol O-acyltransferase (DGAT, EC 2.3.1.20)/*de novo* TAG biosynthesis; (10) phospholipid: diacylglycerol acyltransferase (PDAT, EC 2.3.1.158) and (11) galactolipase (PGD1, EC 3.1.1.26)/alternative acyl donor enzymatic steps for TAG production; (12) betaine lipid synthase 1 (BTA1, no EC number available)/DGTS biosynthesis; and (13) major lipid droplet protein (MLDP, no EC number available)/lipid droplet membrane formation.

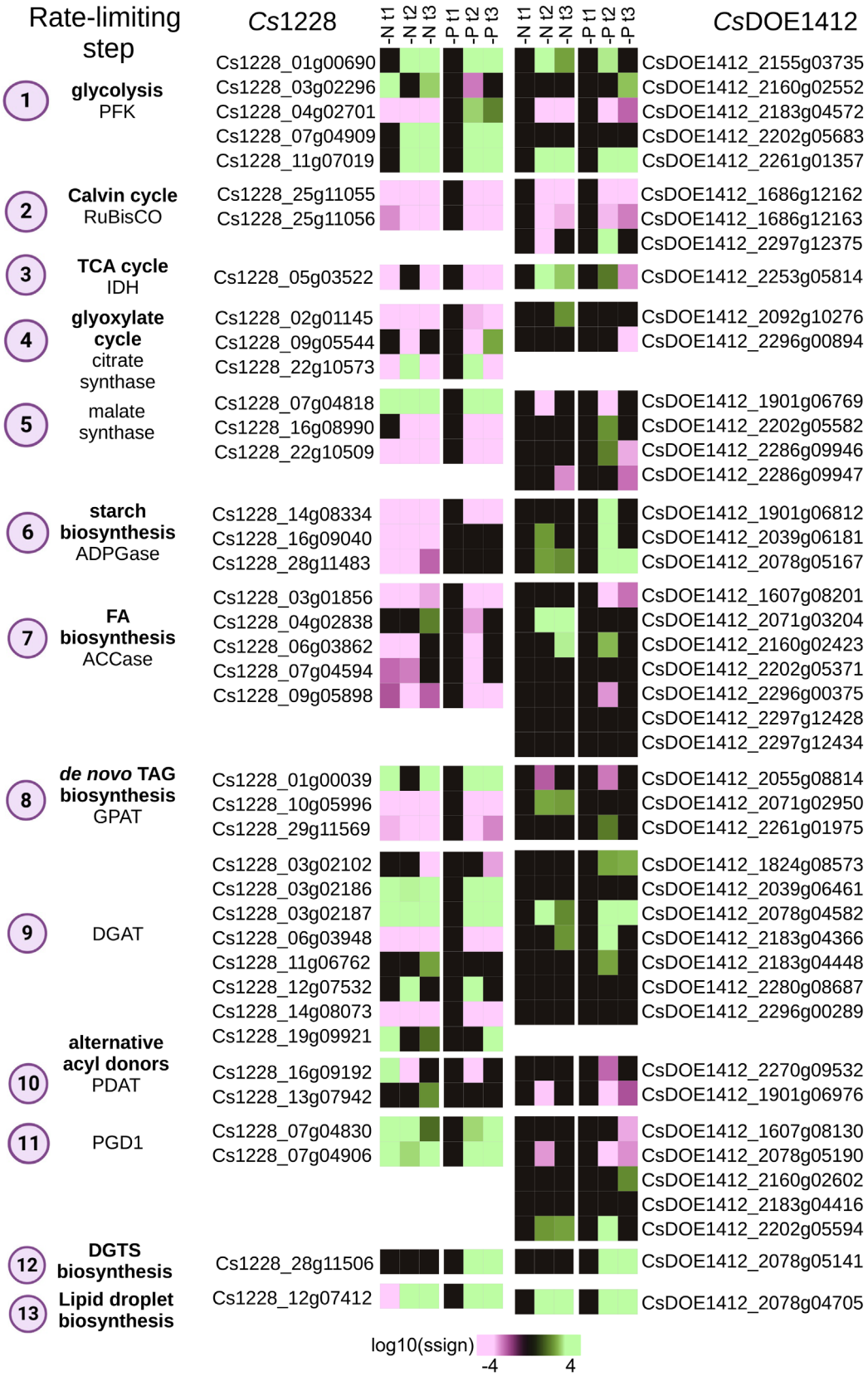

interaction with these TFs in either strain (Figure 7; Data S10). Some TAG-related TFs showed multiple interactions and were inferred to control enzymatic steps in more than one metabolic pathway. Notably, *Cs1228_04g0256* an NF-YC family type TF, potentially controls citrate synthase, DGAT, and BTA1, thus potentially modulating the

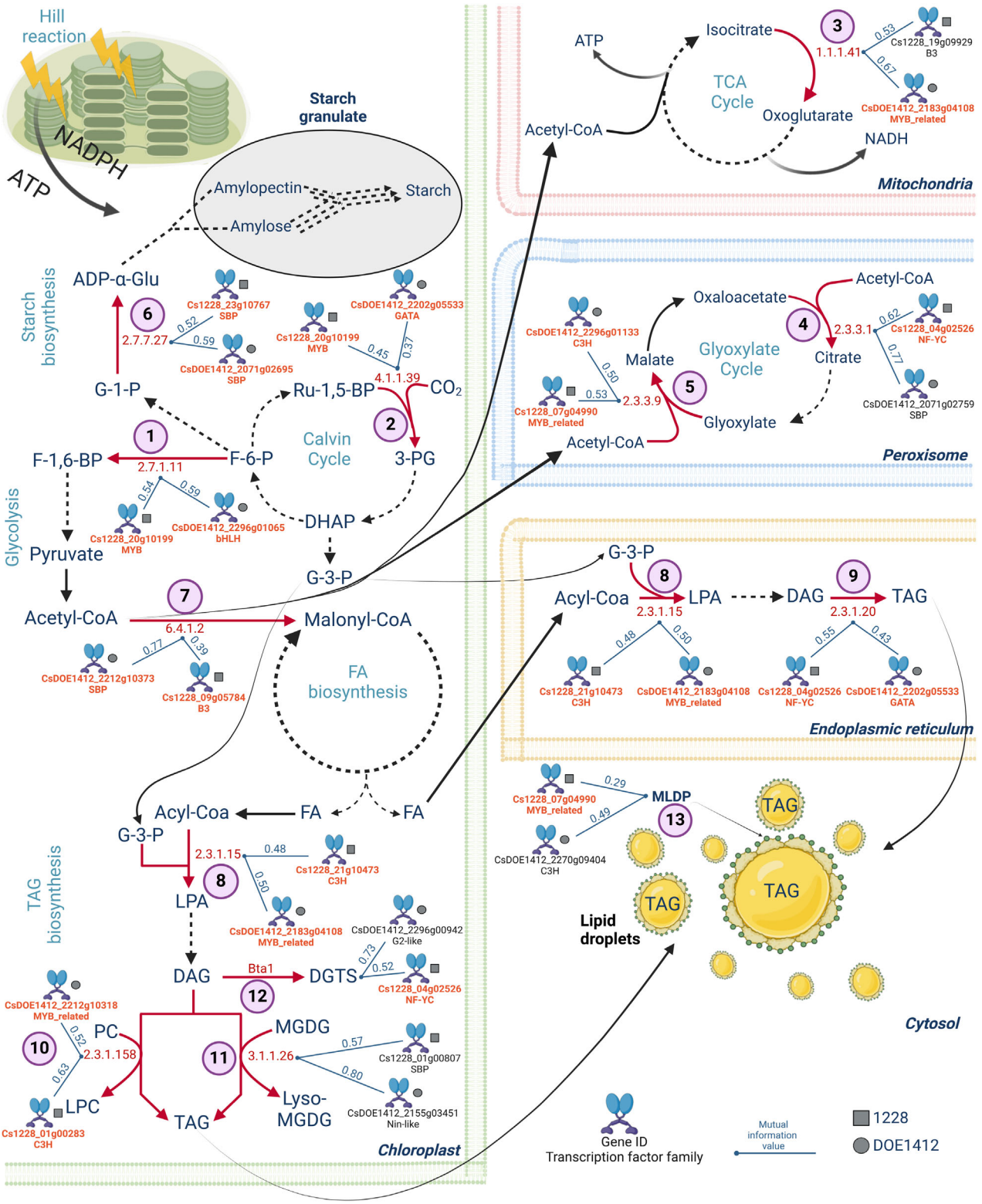

Figure 7. Identification of transcription factors (TFs) controlling rate-limiting steps of global lipid metabolism.
Thirteen rate-limiting steps in the global lipid metabolism were identified from the literature, and the ortholog genes in *Chlorella sorokiniana* UTEX1228 (*Cs*1228) and *C. sorokiniana* DOE1412 (*Cs*DOE1412) were retrieved (see Materials and Methods). The illustration shows the integration of metabolic pathways associated with triacylglycerol (TAG) metabolism, including starch biosynthesis, fatty acid (FA) biosynthesis, glycolysis, TAG biosynthesis and degradation, and the organelles involved. For each of the 13 selected enzymatic steps (numbered in pink circles), the interacting 'TAG-related TFs' are indicated in orange bold letters along with the associated Mutual Information Value. If no 'TAG-related TFs' were identified for an enzymatic step, the TFs with the best Mutual Information Value are indicated in black letters. Solid black arrows indicate a direct metabolic step, dashed arrows indicate several metabolic steps, and solid red arrows indicate rate-limiting steps. 3-PG, 3-phosphoglycerate; ADP-α-Glu, ADP-α-glucose; DAG, diacylglycerol; DGTS, diacylglyceryl-N, N, N trimethylhomoserine; DHAP, dihydroxyacetone phosphate; F-1,6-BP, fructose-1,6-biphosphate; F-6-p, fructose-6-phosphate; FA, fatty acid; G-1-P, glucose-1-phosphate; G-3-P, glycerol-3-phosphate; LPA, lysophosphatidic acid; LPC, lysophosphatidylcholine; Lyso-MGDG, lyso-monogalactosyldiacylglycerol; MGDG, monogalactosyldiacylglycerol; PC, phosphatidylcholine; Ru-1,5-BP, ribulose-1,5-biphosphate; TAG, triacylglycerol. (1) Glycolysis (6-phosphofructokinase, EC 2.7.1.11), (2) Calvin cycle (RuBisCO, EC 4.1.1.39), (3) TCA cycle (Isocitrate dehydrogenase, EC 1.1.1.41), (4, 5) Glyoxylate cycle (citrate synthase, EC 2.3.3.1; malate synthase, EC 2.3.3.9), (6) starch biosynthesis (glucose-1-phosphate adenylyltransferase, EC 2.7.7.27), (7) FA biosynthesis (acetyl-CoA carboxylase, EC 6.4.1.2), (8, 9) *de novo* TAG biosynthesis (glycerol-3-phosphate O-acyltransferase, EC 2.3.1.15; Diacylglycerol O-acyltransferase, EC 2.3.1.20), (10, 11) alternative acyl donor enzymatic steps for TAG production (phospholipid:diacylglycerol acyltransferase, PDAT, EC 2.3.1.158); galactoglycerolipid lipase, (PGD1, EC 3.1.1.26), (12) DGTS biosynthesis (BTA1 homolog, no EC number available), and (13) lipid droplet membrane formation (MLDP, Major lipid droplet protein).

glyoxylate cycle, TAG biosynthesis, and DGTS biosynthesis. Similarly, *CsDOE1412_2202g05533* is a member of the GATA family of TFs that potentially controls the expression of DGAT- and RuBisCO-encoding genes, thus being involved in TAG biosynthesis and the Calvin cycle (Figure 7; Data S10). This suggests that the identified TAG-related TFs likely regulate various biological processes and enzymatic steps on the metabolic global landscape, collectively leading to the observed TAG accumulation in both strains in response to nutrient deficiency.

A similar approach was used to determine whether the RRA top-ranked TFs (Figure 5a,b) interact with these 13 rate-limiting steps of global carbon metabolism. We identified 20 top-ranked TFs with transcriptional interactions across several rate-limiting steps in *Cs*1228, but only three for *Cs*DOE1412 (Data S10). Notably, in *Cs*DOE1412, the Calvin cycle and the biosynthesis of LBs were the metabolic processes found to be regulated by the RRA top-ranked TFs, as we observed interactions with RuBisCO and MLDP-encoding genes. In *Cs*1228, except for the synthesis of DGTS by BTA1, the remaining rate-limiting steps were regulated by RRA top-ranked TFs, including the hydrolysis of MGDG by galactolipase, which did not show any interactions with TAG-related TFs (Data S10). This suggests that the genes associated with TAG metabolism are tightly regulated by a specific set of TFs, whereas primary metabolic pathways are controlled by various TFs with upstream interactions, which collectively contribute to the observed TAG accumulation in both strains in response to nutrient deficiency.

DISCUSSION

Here, we performed comprehensive analyses of two *C. sorokiniana* strains subjected to nutrient stresses, providing detailed insights into their physiological, metabolic, and transcriptional responses associated with TAG accumulation. Our study identified TRNs and TFs that putatively control lipid accumulation in response to —P and —N in *C. sorokiniana*.

While numerous studies have investigated the transcriptional responses to nutrient stress in green microalgae, the comparative framework provided by the *C. sorokiniana* strains *Cs*DOE1412 and *Cs*1228, coupled with the gene coexpression network analysis implemented in this work, enables robust functional prediction of novel TFs involved in lipid metabolism. These TFs, along with previously identified ones, represent valuable resources for genome engineering strategies aimed at enhancing TAG production in green microalgae.

Effects of N and P starvation on cell growth and metabolism

Both —N and —P stresses markedly inhibited growth in *C. sorokiniana*, with concurrent increases in TAG accumulation. *Cs*DOE1412 exhibited more significant growth inhibition and higher TAG levels under both stress conditions, whereas *Cs*1228 demonstrated better tolerance to —P, resulting in lower TAG accumulation (Figures 1 and 2; Figures S2 and S3), possibly due to larger polyphosphate reserves. Similar observations have been reported for *C. reinhardtii* and *C. vulgaris* (Kamalanathan et al., 2015; Moudříková et al., 2017). Growth impairment in both *C. sorokiniana* strains was evident 6-h post-treatment, coinciding with downregulation of DEGs enriched in GO categories related to cell division and DNA replication (GO:0051301 cell division, GO:0006270 DNA replication initiation, GO:0006268 DNA unwinding involved in DNA replication) (Figure 1; Figures S5 and S6). This rapid transcriptional shift contrasts with slower responses reported for *C. reinhardtii*, which maintained growth rates in N-depleted media for up to 24 h, suggesting a more immediate metabolic reprogramming in *C. sorokiniana* (Schmollinger et al., 2014).

In N-deprived cells grown under mixotrophic conditions, the photosynthetic apparatus becomes a target for catabolism due to its high N demand (Yaakob et al., 2021). TEM analysis of both strains revealed pronounced thylakoid disorganization and chloroplast degradation under

—N, accompanied by reduced chlorophyll content and paler culture pigmentation (Figure 1; Figure S1). However, the contrary effect was observed under —P (Figure 1; Figure S1). We found that arginine and glutamine metabolism pathways were enriched across timepoints in —N, underscoring their roles in N storage, remobilization, and stress responses (Figure 3d,e). Arginine possesses the highest N-to-carbon ratio among amino acids and plays a central role in N metabolism as both a storage form of organic N and as a precursor for nitric oxide and polyamines, which are crucial for responses to biotic and abiotic stresses (Winter et al., 2015). Similarly, glutamine is closely associated with N metabolism and is known to facilitate N accumulation and remobilization in higher plants (Cánovas et al., 2018). These responses coincided with enriched GO categories of downregulated genes for both strains in —N, which suggests compromising the photosynthetic machinery (GO:0009765 photosynthesis, GO:0010207 light harvesting, and photosystem II assembly, GO:0015995 chlorophyll biosynthetic process) (Figure S6). Genes encoding the rate-limiting enzyme of the Calvin cycle, RuBisCO, were downregulated in —N in *Cs*1228 (*Cs1228_25g11055*, *Cs1228_25g11056*) and *Cs*DOE1412 (*CsDOE1412_1686g12162*, *CsDOE1412_1686g12163*, *CsDOE1412_2297g12375*) (step 2) (Figure 6). This suggests an early shutdown of CO_2 fixation and redirection of carbon flow toward respiration and lipid biosynthesis. P deficiency has been reported to generally have a lower impact on cell proliferation than N deficiency (Yaakob et al., 2021) and induce a high inter- and intraspecific variability in metabolic responses among the microalgae clade (Chen et al., 2011; Huang et al., 2019; Kamalanathan et al., 2015). In agreement, we found that —P stress caused less severe structural disruptions in both strains, except for the embedding of starch granules (Figure 1e), which correlated with more discrete transcriptional responses (Figures S5 and S6). Notably, one ortholog gene encoding for RuBisCO in *Cs*DOE1412 (*CsDOE1412_2297g12375*) was upregulated under —P, suggesting an alternative mechanism for coping with this stress.

Thylakoid membrane, predominantly composed of SQDG, DGDG, MGDG, and PG, requires a high total content of anionic lipids, specifically PG and SQDG, to maintain the integrity of the photosynthetic apparatus (Kobayashi, 2016). These lipids can substitute for one another to sustain anionic lipid balance in the thylakoid membranes. Our study revealed that SQDG and PG content decreased in both strains under —N stress (Figure 2), potentially destabilizing organelle membranes in N-deprived cells. We observed corresponding decreases in PUFAs, which showed their lowest content under —N treatment for both strains (Table S1). PUFAs have been reported to be enriched in membrane lipids, due to their contribution to membrane fluidity and plasticity under varying environmental conditions (Hawrot-Paw et al., 2021; Yu et al., 2021). In contrast, under —P conditions (t2), MGDG and SQDG contents increased by 126% in *Cs*1228 and 127% in *Cs*DOE1412, while PG decreased slightly. Other lipid components remained unchanged or only slightly affected (Figure 2). This is consistent with known P-stress adaptations in land plants, where galactolipids and sulfolipids, such as SQDG, MGDG, and DGDG, increase in response to —P stress to compensate for reduced phospholipids and maintain membrane stability and function (Bolik et al., 2022). Our results indicate that this trend is common among higher plants and microalgae and is likely to be present in most photosynthetic eukaryotes. PUFAs contents were more abundant under —P compared to —N for both strains, reaching up to 54% of the FAMEs group composition at 48 h in *Cs*DOE1412 (Table 1; Table S1), which correlates with a lipidome comprised by 50% of MGDG and DGTS together at the same timepoint (Figure 2). This suggests a mechanistic link between membrane lipid remodeling and FA desaturation as, under —N, the reduction in thylakoid-associated lipids and diminished desaturase activity restricts PUFA biosynthesis, favoring SFAs and MUFAs (Table 1; Table S1). Conversely, under —P, enhanced synthesis of galactolipids and sulfolipids supports continued plastidial desaturation, leading to a higher proportion of PUFAs as observed previously (Meï et al., 2015; Yu et al., 2021).

Carbon metabolism and TAG biosynthesis

Strain *Cs*DOE1412 was previously highlighted by the National Alliance for Advanced Biofuels and Bioproducts (NAABB) as a promising candidate for biofuel applications (Lammers et al., 2017; Neofotis et al., 2016). NAABB initially isolated *Cs*DOE1412 as a culture contaminant and conducted a detailed characterization of its growth dynamics, biomass, and lipid production potential. *Cs*DOE1412 has been shown to grow very well outdoors in raceway ponds, tolerate a range of salinities and temperatures, and produce up to 30 g m^{-2} day of dried biomass with 25% DCW lipid content with an appropriate FAME profile (Lammers et al., 2017; Neofotis et al., 2016). On the other hand, *Cs*1228 has been poorly characterized in terms of lipid potential compared to *Cs*DOE1412 and other *Chlorella* strains. Our results show that *Cs*DOE1412 is a high TAG producer, in agreement with previous reports, and reveal that strain *Cs*1228 accumulates TAG poorly, even under nutrient stress. *Cs*1228 preferentially accumulates more starch granules (Figure 1e), suggesting a strain unsuitable for biofuel production unless subjected to further improvement. Given that starch synthesis shares common precursors with TAG synthesis (Zhu et al., 2015), carbon flux in this strain appeared to be diverted more evenly between both energy-rich compounds in response to nutrient stress. Nevertheless, since reserve polysaccharides, such

as starch, can serve as sources for biomass conversion technologies via anaerobic digestion (Levasseur et al., 2020), *Cs*1228 is an interesting strain for further investigation in starch-based biofuel production.

The RNA-seq analysis helped us better understand how *Cs*DOE1412 and *Cs*1228 respond to nutrient stress and accumulate TAG. The size and type of the transcriptional responses differed markedly between strains. *Cs*1228 exhibited a more robust transcriptional response with larger sets of DEGs common across nutrient stress treatments and timepoints (Figure 3a,c). *Cs*DOE1412 showed more discrete transcriptional changes with stress-specific responses (Figure 3; Figure S4). This divergence may reflect underlying genomic variation, including differences in TF binding sites and regulatory gene content (Hovde et al., 2018).

With photosynthesis restricted, the demand for energy and reducing equivalents is likely met through central carbon metabolism, utilizing carbon skeletons scavenged from the oxidation of amino acids like lysine and leucine into acetyl-CoA. Although both strains exhibited a similar overall trend in nutrient starvation responses, leading to changes in carbon fluxes and lipid accumulation, *Cs*DOE1412 showed distinct responses at some rate-limiting enzymatic steps, which may help explain its high-lipid content. In both strains, glycolytic flux through the TCA cycle and oxidative phosphorylation appear to support energy demands, as indicated by the upregulation of PFK-encoding genes, the first rate-limiting step in glycolysis, in response to —N and —P conditions (step 1, 6). Glycolysis provides a growing pool of pyruvate that can be converted into acetyl-CoA to support the TCA cycle or directly facilitate the overproduction of FA (Sun et al., 2019). The homolog gene predicted to encode for IDH (step 3) (Figure 7) was downregulated in *Cs*1228 (*Cs1228_05g03522*) in response to —N at all timepoints; in contrast, it was upregulated in *Cs*DOE1412 (*CsDOE1412_2253g05814*) at —N t2, —N t3, and —P t2 when TAG accumulation is evident. This suggests IDH, a rate-limiting enzyme in the TCA cycle, is an important point of control for carbon allocation for lipid biosynthesis in *Cs*DOE1412. On the other hand, most homolog genes encoding citrate synthase and malate synthase, rate-limiting steps in the Glyoxylate cycle (steps 4 and 5) (Figure 7), were either downregulated or only showed slight change under —P t2 and —N t3 in *Cs*DOE1412, whereas in *Cs*1228, malate synthase was upregulated consistently at all timepoints in both stress conditions. This suggests that the glyoxylate cycle has a minor contribution to the metabolic changes and is likely restricted to strain *Cs*1228.

The first and rate-limiting step of the *de novo* FA biosynthesis in the chloroplast is the irreversible conversion of acetyl-CoA into malonyl-CoA by ACCase (Sasaki & Nagano, 2004). In our study, ACCase orthologs in *Cs*1228 were either unchanged or downregulated under both stresses, suggesting limited *de novo* FA biosynthesis. In contrast, *Cs*DOE1412 exhibited upregulation of two ACCase-encoding orthologs in response to —N (t2 and t3) and —P (t2) (step 7) (Figure 6), indicating a strain-specific regulatory pattern that contributes to TAG biosynthesis.

Different routes are known to contribute to the accumulation of TAGs in microalgae. One of them, the acyl-CoA–dependent Kennedy pathway, involves three sequential acylations, finalizing with the step catalyzed by DGAT. Alternatively, the acyl-CoA-independent route, which allows using membrane lipids as acyl donors to produce TAG, is controlled by PGD1 and PDAT that hydrolyze MGDG and PC, respectively (Du et al., 2018). Our results suggest that in *Cs*DOE1412, TAG accumulation takes place predominantly through the acyl-CoA-dependent route under both —P and —N, with a minor contribution from PGD1, whereas in *Cs*1228, both routes appear to be important mainly under —N (Figure 6). Homolog genes putatively encoding for GPAT and DGAT were upregulated under —N and —P at t2 and t3 mainly, in both strains (steps 8 and 9) (Figure 6), correlating with TAG biosynthesis and LB formation (Figures 1 and 2; Figure S2). PDAT homologs were downregulated or showed no expression change in *Cs*DOE1412 under either stress, whereas in *Cs*1228 the two identified homologs were upregulated in response to —N, suggesting a stress-specific response (step 10) (Figure 6). In the case of PGD1 homologs, two out of five (*CsDOE1412_2202g05594*, *CsDOE1412_2160g02602*) were upregulated in *Cs*DOE142 under —N t2, —N t3, or —P t2/t3, whereas in *Cs*1228 all predicted homologs were upregulated at —N (t1, t2, t3) and —P (t2, t3) (steps 10 and 11) (Figure 6). These results correlated with decreased MGDG content at the corresponding timepoints in both strains (Figure 2; Figure S2). TAG accumulation under —N and —P in both strains correlated with consistent upregulation of MLDP-encoding orthologs (*Cs1228_12g07412*, *CsDOE412_2078g04705*), a key structural component of stress-induced LBs (Tsai et al., 2015; Wang et al., 2019) (Figure 6). Taken together, our results suggest that TAG accumulation in *C. sorokiniana* involves stress- and strain-specific responses that combine membrane lipid remodeling and *de novo* biosynthesis.

Betaine lipids accumulate exclusively in response to P starvation

The substitution of phospholipids with betaine lipids as primary membrane components is a well-established adaptive strategy enabling microalgae to withstand P limitation as reported in *Chlorella kessleri* (Oishi et al., 2022), and microalgae on diverse clades, such as *Phaeodactylum tricornotum*, *N. gaditana*, and *Tetraselmis suecica* (Cañavate et al., 2017). Betaine lipids, such as DGTS and diacylglyceryl-carboxyhydroxymethylcholine (DGCC), are

P-free and can functionally replace phospholipids in cellular membranes (Mimouni et al., 2018). In our study, DGTS levels progressively increased from t2 to t3 under —P, ultimately becoming the predominant betaine lipid in both strains (Figure 2). This lipid remodeling coincided with a marked decline in DAG levels, consistent with the upregulation of BTA1-encoding orthologs under —P in *Cs*1228 and *Cs*DOE1412 (Figure 6). BTA1 facilitates the conversion of DAG into DGTS (Riekhof et al., 2005). These findings support the role of BTA1 in DGTS biosynthesis. Of note, the expression of *Bta1*-orthologs was not induced under —N in either strain, and DGTS does not accumulate under this condition, reinforcing the specificity of betaine lipid induction in response to P limitation. The accumulation of DGTS was accompanied by a substantial reduction in PE and PC, the latter being the dominant membrane phospholipid under nutrient-replete conditions (Figure 2; Figure S2). This pattern suggests that PE and PC may serve as sources of FAs and DAG moieties for DGTS biosynthesis.

Additionally, diacylglyceryl glucuronide (DGGA) was exclusively detected in *Cs*DOE1412 under control conditions and further enhanced in response to —P (Figure 2; Figure S2). While DGTS are found in various algae, plants, and fungi (Mühlroth et al., 2017), DGCC has been identified thus far only in dinoflagellates (Canãvate et al., 2016), highlighting species-specific adaptations in betaine lipid utilization.

Gene-coexpression networks reveal TF-target gene interactions regulating response to nutrient stress and timing

The TRNs constructed for *C. sorokiniana*, FullNet_Cs1228 and FullNet_CsDOE1412, revealed a high density of regulatory nodes, surpassing comparable networks for *C. reinhardtii* (Romero-Campero et al., 2016). We identified both shared and strain-specific gene communities, including conserved modules enriched in DNA replication, protein phosphorylation, autophagy, N metabolism, and membrane transport (Figure S11). Top-ranked TFs (Figure 5a,b) were centrally positioned in their respective modules, reinforcing their predicted regulatory importance.

Of particular interest were conserved gene communities related to nitrogen transport and arginine biosynthesis in the TRN, consistent with enrichment of related GO terms (e.g., 'GO:0042450 arginine biosynthetic process') among upregulated DEGs under —N across all timepoints in both strains (Figure 3d,e). Conserved transcriptional circuits further supported a coordinated response to —N across both strains (Figure S15), recapitulating major components of previously described nitrogen stress responses in plants and microalgae. In contrast, transcriptional regulation under —P diverged significantly between strains (Figure 1; Figure S5), with only limited conserved transcriptional interactions detected at t2 (Figure S15). We identified in both strains orthologs of the PHOSPHATE STARVATION RESPONSE 1 (PHR1) TF, the central regulator of the phosphate starvation response in plants (Bustos et al., 2010). In *Cs*DOE1412, the PHR1 ortholog, *CsDOE1412_2296g00942*, was strongly induced (up to 10-fold) at both early and late-P timepoints, whereas in *Cs*1228, the PHR1-ortholog *Cs1228_02g01109* was modestly upregulated (~2-fold) (Figures S17 and S18). This differential expression correlated with *Cs*DOE1412's stronger —P phenotype, including greater growth inhibition and TAG accumulation. The predicted targets of PHR1 differed markedly between strains. In *Cs*DOE1412, PHR1 targeted canonical effectors such as H^+/Pi cotransporters, phosphate transporters, and SPX-domain-containing proteins (Figure S17) (Kumar Sharma et al., 2020; Wang et al., 2021), in line with enriched GO terms specific to —P like 'GO:0016036 cellular response to phosphate starvation' exclusively in upregulated DEGs. In contrast, in *Cs*1228 PHR1 targets included photosynthetic and cell cycle genes (downregulated), and carbohydrate biosynthesis genes (upregulated), consistent with increased starch granule accumulation under —P (Figure 1e; Figure S5a). These findings indicate that, despite conservation of PHR1, its transcriptional circuitry is rewired in the two strains, likely reflecting adaptive divergence in resource allocation under —P. Interestingly, although PHR1 is considered constitutively expressed in higher plants (Wang et al., 2021), it was transcriptionally induced under —P in both *C. sorokiniana* strains, suggesting additional layers of transcriptional control that activate phosphate starvation responses in microalgae.

The TAG-related subnetworks allowed us to identify TFs potentially regulating TAG accumulation in response to nutrient stress in *Cs*1228 and *Cs*DOE1412 (Figure S16). We focused on TFs with differential expression in conditions of high TAG content, specifically during —N t2 and —N t3, and —P t2. Among the 14 TFs identified in *Cs*1228 and 15 in *Cs*DOE1412 (Figure 5e), only three have orthologs in the other strain. This suggests that TAG accumulation involves both conserved and unique transcriptional regulators. We identified TAG-related TFs belonging to families that have not been previously reported to regulate TAG accumulation in microalgae, such as NF-YC, B3, and M-type MADS in *Cs*1228, and Whirly in *Cs*DOE1412. These TFs represent novel candidates for genome engineering strategies to improve TAG accumulation in microalgae. The notion of the bona fide role of the novel TAG-related TFs identified in this work is supported by the finding that our analysis included several TAG-related TFs that shared homology with TFs demonstrated to be involved in lipid accumulation and controlling responses to —N or —P stresses in other microalgae or higher plants (Figure 5). For instance, orthologs of GmZF351 and GmZF392 in *Glycine max* (Romero-Campero et al., 2016); WRINKLED 1 in *Arabidopsis thaliana* and *G. max* (Cernac & Benning, 2004; Chen

et al., 2018); NoAP2 (AP2) in *N. oceanica* (Südfeld et al., 2021); ApMYB6 (MYB) in *A. protothecoides* (Xing et al., 2021); NRR1 (SBP) and PSR1 (G2-like) in *C. reinhardtii* were identified in our TRN analysis (Bajhaiya et al., 2016; Boyle et al., 2012).

C3H-type TF-encoding orthologs (*CsDOE1412_2296g01133*, *CsDOE1412_2079g0*, *Cs1228_21g10473*, *Cs1228_02g00899*) were upregulated in both strains (Figure 5e), which suggests that transcriptional pathways for TAG accumulation are conserved, while others have been rewired, leading to important differences in the magnitude and timing of the nutritional stress response. This difference in transcriptional regulation is also reflected in the limited number of significantly scored TFs found in the DEGs_Subnet(s) of *Cs*DOE1412, in contrast to *Cs*1228, which displayed a more extensive response involving a larger set of TFs and common interactors (Figure 5a–d).

Overall, these findings point to complex transcriptional circuits where TAG-related TFs and other central regulators synergistically control multiple metabolic processes in response to stress, ultimately leading to TAG accumulation. Exploring how rational rewiring of these TAG-regulatory networks could enhance natural diversity and accelerate the domestication of microalgal strains and species with lipid production potential, such as *Chlorella*, would be particularly valuable. Future studies utilizing knockout mutants or overexpression lines could further elucidate the interactions presented here and functionally validate the roles of these TFs as key regulators of nutrient stress responses.

MATERIALS AND METHODS

Strains and culturing conditions

This study used two *C. sorokiniana* strains, DOE1412 and UTEX1228, which were obtained from the Culture Collection of Algae at The University of Texas at Austin (UTEX, www.utex.org). Cultures were grown mixotrophically on TAP media. The following stock solutions were prepared: Beijerinck's, phosphate buffer, Hunter's trace, and tris acetate, following UTEX recipe and preparation instructions. In this recipe, the N source is NH_4Cl from Beijerinck's solution, and the P source is a combination of Na_2HPO_4 and KH_2PO_4 from the phosphate buffer. Freshly prepared nutrient-sufficient media (Ctl) contained 116.43 ppm of NH_4^+ and 27.22 ppm of PO_4^{-3} as determined by IC. For —N and —P experiments, TAP media recipe was modified accordingly. For —N condition, the Beijerinck's solution did not contain the inorganic N source. For the —P condition, the phosphate buffer stock solution was omitted when preparing the final media; thus, the P sources were completely absent. Cultures were maintained at constant shaking (140 rpm) in a Conviron growth chamber (MTR30 model, Conviron, USA) at 25°C, with a 12-h light/12-h dark photoperiod and illumination provided by white fluorescent lights at ~150 μmol photons m^{-2} sec^{-1}. Similar growth conditions were established for all experiments under —N and —P stress conditions.

Nutrient stress experiments

Seed cultures were inoculated 24 h before performing nutrient stress experiments, so they were in the exponential growth phase. Exponential growth was confirmed by measuring cell concentration at inoculation and at 6-h intervals. Cell counting was performed manually with a Neubauer chamber (Countess II FL, Life Technologies, Carlsbad, CA, USA) or using an automatic cell counter with reusable slides (Countess 3 FL, Invitrogen, Carlsbad, CA, USA). Experimental flasks were inoculated from the seed culture to an initial cell concentration of 1×10^7 cells ml^{-1}, with a final volume of 50 ml, in TAP media Control, —N and —P. The calculated inoculum volume from the seed culture was centrifuged at 4000 ***g*** for 5 min at room temperature. The supernatant was discarded, and then, three washes with the corresponding treatment media were performed on the pellet to remove traces of the nutrient-replete media from the cells. After the washing steps, pellets were resuspended and inoculated into their corresponding experimental treatment media. Experimental cultures were grown in triplicate and randomly distributed on the shaker (Innova 2100, New Brunswick Scientific Co., Enfield, CT, USA) within the growth chamber to minimize errors from uneven light or temperature distribution.

Culture growth was measured by optical density (OD) at 680 nm (OD_{680}) using a Spark® microplate reader (TECAN, Grodig, Austria). About 200 μl were taken directly from the experimental culture and transferred into a well of a 96-well plate. Each growth point represented the mean of three biological replicates, with four technical replicates each.

Chlorophyll quantification

Chlorophyll quantification was conducted spectrophotometrically using a solvent extraction method and the Spark® microplate reader (TECAN, Grodig, Austria) to determine absorbance. For chlorophyll extraction, 5 ml of experimental cell culture was centrifuged at 4000 ***g*** for 10 min, and the supernatant was discarded. Next, the pellet was resuspended in two volumes of a 1:1 mixture of acetone (Cat. No. 320110, Sigma-Aldrich, St. Louis, MO, USA) and DMSO (Cat. No. 472301, Sigma-Aldrich) by vigorous vortexing to ensure suspension before transferring the sample to a glass vial and incubating in a water bath at 50°C for 30 min in the dark. Samples were centrifuged as indicated earlier, and the absorbance of 200 μl of the supernatant was immediately measured. Chlorophyll content was calculated using absorbance at 648, 666, and 750 nm according to the extinction coefficients and formulas described previously for *Chlorella* (Ritchie et al., 2021).

Transmission electron microscopy

For TEM imaging, we followed the standard protocol: a biomass pellet was prepared from experimental cultures at the established timepoints and fixed in a 2% v/v glutaraldehyde ($C_5H_8O_2$) solution in 0.1 M sodium cacodylate [$(CH_3)_2AsO_2Na{\cdot}3H_2O$] buffer (pH 6.8–7.2) for 1 h. Then, three washes with cacodylate buffer were performed. Next, a post-fixation with 1% (w/v) osmium tetroxide (OsO_4) for 1 h was followed by three washes with the same buffer. The sample was then dehydrated through an increasing ethanol series and a final wash with acetone in a shaker for 15 min. Then, serial incubations of 1 h with acetone: resin (LX-112 resin, LADD Research Industries, Williston, VT, USA) at the following proportions: 4:1, 1:1, and 1:4, to finalize with 100% resin incubation at 60°C for 48 h. Embedded specimens were then used to produce ultrathin sections (<60 nm) on an ultramicrotome PowerTome PC (RMC Boeckeler, Tucson, AZ, USA), which were then mounted on

formvar-coated copper TEM grids and stained with uranyl acetate and lead citrate. Examination was performed with H-7650 TEM (Hitachi, Tokyo, Japan) with HV of 60 kV.

RNA extraction

Biomass samples were harvested at the three established time-points (t1, t2, t3). The complete volume of the liquid culture (50 ml) was transferred to a sterile centrifuge tube, and the biomass was centrifuged at 4000 ***g*** at room temperature for 10 min. Then, the supernatant was carefully discarded, and the pellet was immediately flash-frozen with liquid nitrogen. Frozen pellets were quickly ground into a fine powder using a vertical mixer homogenizer (High-Torque Brushless Mixer, Caframo, Wiarton, ON, Canada). Approximately 100 mg of fine powder was used for RNA extraction with the Direct-zol® RNA extraction kit from Zymo Research (Cat. No. R2051, Irvine, CA, USA) following the manufacturer's instructions. For samples exposed to longer stress treatment (48 h, t3), the increased cellular lipid content interfered with RNA extraction with this kit. These samples were extracted using the protocol based on TRIzol™ and chloroform, as described in the ThermoFischer TRIzol™ reagent user guide (Cat. No. MAN0001271 B.0) and then combined with the Direct-zol® RNA extraction kit for nucleic acid purification. To assess the quality of extracted RNA, a spectrophotometer ND-1000 (Nano Drop Technology, Wilmington, DE, USA) was used, and only samples with A260/A280 and A230/A280 greater than 2.0 were used for further sequencing. Three hundred nanogram of total RNA were also run on a 1.2% agarose electrophoresis gel (Cat. No. 16500-500, Invitrogen) to visually confirm integrity and purity. Samples that passed the quality control were used for library preparation. Libraries were sequenced using the Illumina HiSeq 2000 platform with paired-end 150 bp reads at Novogene Corporation Inc. (Sacramento, CA, USA).

RNA-seq and GO analysis

For quality assessment of the resulting raw sequencing reads, we used FastQC tool (version 0.11.9, https://www.bioinformatics.babraham.ac.uk/projects/fastqc/) with default settings. High-quality reads were pseudo-aligned with RNA-seq quantification program kallisto (version 0.46.1) (Bray et al., 2016), using *Cs*DOE1412 and *Cs*1228 genome assemblies (Hovde et al., 2018) as the reference genomes for the corresponding strain. Next, calculated abundances at the gene level were integrated into count-based statistical analysis in edgeR (version 3.13) (Robinson et al., 2010) and DEseq2 (version 3.13) (Love et al., 2014) using the tximport R package (Soneson et al., 2015). To determine DEGs, we established a false discovery rate cutoff threshold (FDR $\leq$0.01) for every contrast evaluated here. Additionally, a design matrix was created to fit the conditions assessed. We formulated two different contrasts to evaluate responses to stress treatments. Different versions of the contrasts for every condition are indicated (Data S3, 'V2'). Quantitative intersection analysis between DEG sets among treatments was performed with UpSetR package version 1.4 for the R environment (Conway et al., 2017). DEGs, considered statistically significant, were used to perform GO analysis with the topGO package for the R environment (Alexa & Rahnenfuhrer, 2010); a *P*-value cutoff of $P \leq 0.01$ was set for GO terms analyzed. We used the assigned *P*-value to create heatmaps using the ComplexHeatmap R package (Gu et al., 2016) and bubble plots with the ggplot2 R package (Wickham, 2016).

Hierarchical clustering analysis

To perform clustering analysis, we first calculated the TPM mean for each treatment triplicate and gene. Next, we used TPM mean values to calculate z-scores for each gene across samples, using the scale function in the R base package. We calculated the distance matrix using the Ward.D2 linkage method in the hclust R base function and made the cut in five clusters for both strains. Then, we used the ggplot2 R package (Wickham, 2016) to plot the *z*-score trends and the mean trend in each cluster.

TRN and DEGs subnetworks inference and analysis

Regulatory networks of coexpression were inferred using ARACNe's algorithm (Margolin, Wang, et al., 2006). We used as input the calculated expression value matrix, in TPM units, for all expressed genes of every RNA-seq library and a list of TFs for each species obtained using the TF Prediction module from PlantTFDB (Tian et al., 2020). The ARACNe algorithm infers interactions among genes in pairwise comparisons of their expression profiles across all conditions considered in the experiments. Thus, an adjacent matrix of interacting pairs is generated, ranked by a calculated Mutual Information (MI) value and its associated *P*-value. The resulting matrix was visualized as a graph, showing TFs and non-TFs coding genes as nodes connected by edges relative to their calculated interactions based on MI values (Margolin, Wang, et al., 2006). In a biological context, in any given paired interaction, if one gene is a TF-coding gene and the other is non-TF coding, then it is assumed that this TF is a transcriptional regulator of the other.

We inferred global GRNs for each species, a network of TFs-only genes (tfsnet), and a network of TFs-to-noTFs (notfsnet), using a DPI value of 0.0 and a threshold MI value of 0.1. The tfsnet and notfsnet were merged to obtain the complete GRN (Fullnet). This was used to create subnetworks for —N and —P DEGs using the subnetwork function from the igraph package for R environment (Csardi & Nepusz, 2014). Then, DEGs expression values were mapped to the subnetworks for each treatment using gene identifiers (DEGs_Subnet). To analyze these subnetworks, we employed five centrality measures: degree, closeness, betweenness, eigenvector, and PageRank as implemented in the igraph package. We then integrated the scores using the RRA algorithm, implemented in the RobustRankAggreg R package (Kolde et al., 2012). Thus, we identified the top-ranked nodes for every DEGs_Subnet. Next, using the list of top-ranked nodes (which were genes coding for TFs), we used the neighbor's function from the igraph package to retrieve their first interactors on each DEGs_Subnet for Venn diagram analysis using ggvenn function (Linlin, 2023). Each generated intersection was evaluated for enrichment in GO biological processes categories with the topGO algorithm.

We also obtained, for each species, the minimum spanning tree of the tfsnet and retrieved the Louvain community memberships using the mst function from igraph package. Then, for each noTF gene in the notfsnet, we retrieved the edge with the highest MI, and its corresponding 'best' TF, and assigned the noTF to the gene community. All noTF genes inherited the community membership of their highest MI TF. This resulted in non-overlapping lists of noTFs interactors for each TF, which were analyzed for enrichment of GO biological process categories with the topGO algorithm.

Orthogroup subnetworks inference

The gene identifiers in each list of DEGs for each species and each contrast were converted to orthogroup identifiers from our N0 output table produced by running Orthofinder with the protein fasta files from both species as input (Emms & Kelly, 2019). We then obtained, for each contrast in which both species had DEGs, that is, —N t2, —N t3, —P t2, and —P t3, the subnetwork of

differentially expressed orthogroups. At this point, we had two subnetworks per contrast, one for each species. For each contrast, we obtained the subnetworks intersection, representing the transcriptional regulatory interactions shared between both datasets and potentially conserved between both strains in a specific condition. The list of orthogroups for each interaction was then used as input to topGO to identify the enriched GO biological process categories represented in each intersection network.

Enzyme annotation with E2P2

To functionally characterize the gene sets from both *C. sorokiniana* strains, we first retrieved the CDS from each mRNA sequence using a custom Pearl script. Next, we used TranSeq (Transeq, RRID:SCR_015647) to translate the nucleic acid sequences to their corresponding peptide sequences. We used this file as input to the E2P2 pipeline (Schläpfer et al., 2017), which identifies the peptides by sequence and annotates them based on their catalytic functions using the four-part Enzyme Commission (EC) number system. Thus, each peptide was assigned an EC number, producing an E2P2 dataset for each strain.

TAG-related subnetworks

From our E2P2 data, we retrieved all identifiers for genes belonging to the FA biosynthesis, TAG biosynthesis, TAG degradation, starch biosynthesis, and starch accumulation pathways. This list was filtered to keep only DEGs, upregulated for FA biosynthesis, TAG biosynthesis, and starch degradation, and downregulated for TAG degradation and starch biosynthesis in —N t2 and/or —N t3 and/or —P t2. The filtered gene list was used to retrieve from the Fullnet, for each species, the gene's first neighbors, which are TFs. The resulting subnetwork represents the potential TRN involved in TAG accumulation.

Identification of TFs regulating rate-limiting steps in carbon metabolism

Based on the literature, we identified the rate-limiting steps in glycolysis (Chaudhry & Varacallo, 2018), Calvin cycle (Sharma et al., 2020), TCA cycle (Zhang & Fernie, 2023), glyoxylate cycle (Theodoulou & Eastmond, 2012), starch biosynthesis (Bahaji et al., 2014), FA biosynthesis (He et al., 2020), *de novo* TAG biosynthesis (Fukuda et al., 2018), and alternative enzymatic steps for TAG production (Du & Benning, 2016), as these pathways are likely involved in the TAG accumulation response. Next, we used the EC numbers assigned to the rate-limiting steps and located them in the E2P2 datasets to retrieve the genes encoding those enzymes in our strains. Our E2P2 datasets did not contain any protein classified as EC 2.3.1.158 phospholipid:diacylglycerol acyltransferase. However, enzymes with this EC number contain a Lecithin: cholesterol/-phospholipid:diacylglycerol acyltransferase domain, IPR003386 in the InterPro database (Paysan-Lafosse et al., 2023). We searched our InterProScan results for proteins with this domain and found Cs1228_13g07942 and Cs1228_16g09192 for *Cs*1228, and CsDOE1412_1901g06976 and CsDOE1412_2270g09532 for *Cs*DOE1412. Also, no EC number was assigned to the DGTS biosynthesis step. Therefore, we used the well-studied gene *Bta1* that encodes the enzyme catalyzing this reaction in *C. reinhardtii*, to look for orthologs in our *C. sorokiniana* strains. We found Cs1228_28g11506 for *Cs*1228 and CsDOE1412_2078g05141 for *Cs*DOE1412. An overview of the metabolic landscape drawn from the genes identified as rate-limiting steps on the selected pathways and their sign significance is presented. Next, we retrieved each gene's TF interactors from the FullNet networks.

Neutral lipid extraction and FAMEs quantification

The biomass of both *C. sorokiniana* strains was harvested as described above and then freeze-dried using a FreeZone Freeze Dryer (Labconco, Kansas, MO, USA). Lyophilization was performed at 0.02 mbar with a collector temperature of −88°C overnight. Total lipid extraction was performed by weighing 10 mg of the freeze-dried biomass for each stress condition and timepoint individually. About 4 ml of a 1:1 chloroform:methanol mixture (Cat. No. 366927 and 676780, Sigma-Aldrich, St. Louis, MO, USA) was then added to the biomass in a glass vial, vortexed vigorously, and subsequently sonicated at 35 kHz for 15 min. The solvent-debris mixture was transferred to a centrifuge tube for centrifugation at 3850 ***g*** for 5 min. Two volumes of 1.5 ml from the upper phase were transferred to two separate glass vials and subjected to a constant stream of nitrogen until the extracted lipids were completely dried from the solvent. The two vials were used for total neutral lipid and FAMEs analyses. For the identification and quantification of total neutral lipids, the dried extracted lipids contained in one vial were resuspended in 500 μl of a 1:9 chloroform:methanol mixture by aspiration and then filtered through a 0.2 μm syringe filter for injection into a UHPLC coupled with mass spectrometry (see the next section for chromatographic method details). Dried extracted lipids from the second vial were used for transesterification to FAMEs following a method modified from (Breuer et al., 2013). First, extracted dried lipids were resuspended with 500 μl of methanol (Cat. No. 676780, Sigma-Aldrich) containing 5% (v/v) sulfuric acid and transferred to a microcentrifuge tube. Samples were incubated for 3 h at 70°C in a thermal block (PCMT Thermoshaker, Grant-bio, Cambridge, UK) with constant shaking at 450 rpm. The tubes were then cooled to room temperature. Next, 500 μl of Mili-Q water and 500 μl of hexane (Cat. No. H292-4, Fisher Scientific, Waltham, MA, USA) were added, followed by mixing at room temperature for 15 min at 1500 rpm. Then, they were centrifuged at 3850 ***g*** for 5 min, and 350 μl from the upper hexane phase were collected and transferred to a new tube. A washing step was performed by adding the same volume of Mili-Q water and centrifuging as indicated. Finally, the upper phase was collected and transferred to a glass vial for its subsequent injection into a GC instrument coupled to a mass spectrometer.

UHPLC–MS and GC–MS analyses

We used a reversed-phase methodology for the chromatographic separation of neutral and polar lipids. Accucore™ Vanquish C18+ UHPLC column was used (50 × 2.1 mm, 1.5 μm) in a Vanquish Flex UHPLC. For the mobile phases, we used water 0.1% formic acid (A), and 2 mM ammonium formate (Cat. No. 70221-25G-F, Sigma-Aldrich), isopropanol MS grade (A464-4, Fisher Scientific) (B). The gradient used was 5% B, 0–2 min; 5–100% B, 2–12 min; 100% B, 12–14 min; 100–5% B, 14–14.1 min; 5% B, 14.1–17 min. Detection was performed using an Orbitrap Exploris 240 mass spectrometer (Thermo Scientific, Waltham, MA, USA) equipped with H-ESI. Both positive and negative ionization modes were used to detect neutral and polar lipids. For FAME detection, samples were analyzed using a TRACE 1310 gas chromatograph coupled to an ISQ7000 mass spectrometer (Thermo Scientific). Separation was achieved using a TRACE TR-FAME GC column (10 m × 0.1 mm × 0.2 μm) with ramped temperature from 40°C to 150°C at 80°C min^{-1}, and from 150°C to 240°C at 8°C min^{-1}. Helium flow was maintained at a constant rate of 0.350 ml min^{-1}. One microliter of either sample or the FAME standard was injected into the chromatography inlet, maintained at 220°C, using split mode with a ratio of 251:1. Calibration curves and data

analysis were performed using Chromeleon Chromatography Studio (Thermo Scientific).

IC analysis

To quantify the N source (NH_4Cl) and P source (Na_2HPO_4 and KH_2PO_4) concentrations in the nutrient-sufficient media (control) at 6 and 48 h of incubation, separate experiments to grow both strains, *Cs*DOE1421 and *Cs*1228, were performed. Cultures were set up in triplicate and harvested by centrifugation at 4000 ***g*** for 10 min. Then, 5 ml was collected from the upper part of the supernatant and filtered using 0.22 μm syringe filters (Biomed Scientific, Los Angeles, CA, USA) to remove residual cells. These supernatants were used for injection and analysis. TAP growth medium was also analyzed prior to cell inoculation to determine the baseline levels of both nutrients. Both ions' concentrations were quantified by suppressed-conductivity ion chromatography using a Dionex Inuvion IC system (Thermo Scientific). For anion analysis, separations were performed isocratically on a Dionex IonPac AS11-HC column (4 × 250 mm) at a flow rate of 1.0 ml min^{-1} with a 32 mM KOH eluent, column temperature of 30°C, and suppressor current of 80 mA. For cation analysis, separations were conducted on a Dionex IonPac CS12A column (4 × 250 mm) at a flow rate of 1.0 ml min^{-1} using a 48 mM methanesulfonic acid eluent, column temperature of 35°C, and suppressor current of 141 mA. Calibration was performed with NH_4Cl and KH_2PO_4 standards; method blanks and spike recoveries were included for quality control. Quantifications were performed with four technical replicates for each biological replicate.

ACKNOWLEDGMENTS

We thank Luis Herrera-Estrella and Lam-Son Phan Tran for their critical reading of the manuscript. We are grateful to Alethia Brito-Bello for her support with RNA extraction and culture handling, to Stephanny Lizarraga for her assistance with TEM methods, and to Francisco Perez-Zavala for his advice on bioinformatic analysis and help with data submission to NCBI. We also thank Brad Thornhill for his support with Ion Chromatography analysis. This work was partially supported by the National Science Foundation, US, under the award number 2442462 to DL-A.

AUTHOR CONTRIBUTIONS

DL-A: conceived and coordinated the project; DL-A and CCB-D: designed the experimental plan; CCB-D, DL-A, and RACM: executed experimental work and performed data analysis and interpretation; RACM and CCB-D: designed the computational analysis and performed analytics; H-RN-G, CCB-D, and RACM: established lipidomics protocols and chromatography methods and performed analytics; CCB-D, RACM, and DL-A: designed figures; CCB-D: wrote the first draft of the manuscript; CCB-D, RACM, and DL-A: writing and review. DL-A: funding acquisition. All authors commented on, discussed, and agreed upon the final manuscript.

CONFLICT OF INTEREST

The authors declare that there are no conflicts of interest.

DATA AVAILABILITY STATEMENT

The RNA-seq data underlying this article are available online in the National Center for Biotechnology Information (NCBI) Sequence Read Archive (SRA) database and can be accessed with the accession number PRJNA1272067.

SUPPORTING INFORMATION

Additional Supporting Information may be found in the online version of this article.

Figure S1. Effects of nitrogen and phosphorus starvation on chlorophyll contents of *Chlorella sorokiniana* strains.

Figure S2. Abundance of major lipid classes in *C. sorokiniana* strains in response to phosphorus and nitrogen starvation.

Figure S3. Fatty acid (FA) composition of triacylglycerols (TAGs) in *C. sorokiniana* strains in response to nutrient stress.

Figure S4. Transcriptional responses induced by phosphorus and nitrogen starvation stress in *C. sorokiniana* strains.

Figure S5. Gene Ontology (GO) enriched functional categories of upregulated differentially expressed genes (DEGs) in *C. sorokiniana* strains in response to phosphorus stress.

Figure S6. Gene Ontology (GO) enriched functional categories of downregulated differentially expressed genes (DEGs) in *C. sorokiniana* strains in response to nitrogen stress.

Figure S7. Gene Ontology (GO) enriched functional categories of downregulated differentially expressed genes (DEGs) in *C. sorokiniana* strains in response to phosphorus stress.

Figure S8. Differentially expressed genes (DEGs) analysis under different treatments and timepoints relative to the earliest timepoint control condition (Ctl t1).

Figure S9. Transcription factors (TFs) show diverse expression patterns in response to stress conditions.

Figure S10. Transcription factors (TFs) response to nutrient starvation in *C. sorokiniana* strains.

Figure S11. Minimum spanning tree of transcriptional regulatory networks in *C. sorokiniana* strains (mst_net).

Figure S12. Subnetwork of differentially expressed genes (DEGs_Subnet) in response to nutrient stress in *C. sorokiniana* UTEX1228.

Figure S13. Subnetwork of differentially expressed genes (DEGs_Subnet) in response to nutrient stress in *C. sorokiniana* DOE1412.

Figure S14. First-level interactors of the top-ranked transcription factors (TFs) in DEGs_Subnet show enrichment of conserved and unique biological processes in *C. sorokiniana* strains.

Figure S15. Conserved gene regulatory networks between *C. sorokiniana* UTEX1228 (*Cs*1228) and *C. sorokiniana* DOE1412 (*Cs*DOE1412).

Figure S16. Expression profile of transcription factors controlling enzymatic steps of pathways directly influencing TAG accumulation in *C. sorokiniana*.

Figure S17. Regulatory node controlled by the PHR1-ortholog in *C. sorokiniana* DOE1412 (*Cs*DOE1412).

Figure S18. Regulatory node controlled by the PHR1-ortholog in *C. sorokiniana* UTEX1228 (*Cs*1228).

Table S1. Fatty acid methyl ester (FAME) content (μg g^{-1} dry biomass) in *Cs*1228 and *Cs*DOE1412 under different conditions.

Table S2. Description of inferred transcriptional regulatory networks and subnetworks using Aracne.

Data S1. Ion chromatography data for both *C. sorokiniana* strains in control conditions.

Data S2. Lipidome data for both *C. sorokiniana* strains under different stress conditions.

Data S3. Differential expression analysis for both *C. sorokiniana* strains under −N and −P at three timepoints.

Data S4. Time and treatment-specific DEGs for both strains under different nutrient stress treatments and timepoints.

Data S5. Gene Ontology (GO) enrichment analysis for DEGs.

Data S6. Transcription factor hierarchical clustering analysis.

Data S7. Non-redundant adjacency matrix (or transcriptional regulatory network, TRN) generated from RNA-seq data for TF coding and non-TF coding genes.

Data S8. Gene Ontology (GO) enrichment analysis of first interactors of the top-ranked TFs through the DEGs_Subnet in both strains.

Data S9. Orthogroups generated from transcriptional regulatory interactions conserved between *Cs*1228 and *Cs*DOE1412.

Data S10. Transcriptional interactions of genes encoding rate-limiting steps of carbon metabolism with TFs on the respective strains FullNet networks.

REFERENCES

Adams, C., **Godfrey, V.**, **Wahlen, B.**, **Seefeldt, L.** & **Bugbee, B.** (2013) Understanding precision nitrogen stress to optimize the growth and lipid content tradeoff in oleaginous green microalgae. *Bioresource Technology*, **131**, 188–194. Available from: https://doi.org/10.1016/J.BIORTECH.2012.12.143

Alexa, A. & **Rahnenfuhrer, J.** (2010) topGO: enrichment analysis for gene ontology. R package version, 2(0).

Aoki, K., **Ogata, Y.** & **Shibata, D.** (2007) Approaches for extracting practical information from gene co-expression networks in plant biology. *Plant and Cell Physiology*, **48**(3), 381–390. Available from: https://doi.org/10.1093/PCP/PCM013

Bahaji, A., **Li, J.**, **Sánchez-López, Á.M.**, **Baroja-Fernández, E.**, **Muñoz, F.J.**, **Ovecka, M.** ***et al.*** (2014) Starch biosynthesis, its regulation and biotechnological approaches to improve crop yields. *Biotechnology Advances*, **32**(1), 87–106.

Bajhaiya, A.K., **Dean, A.P.**, **Zeef, L.A.H.**, **Webster, R.E.**, **Pittman, J.K.**, **Performed, R.E.W.** ***et al.*** (2016) PSR1 is a global transcriptional regulator of phosphorus deficiency responses and carbon storage metabolism in *Chlamydomonas reinhardtii*. *Plant Physiology Ò*, **170**, 1216–1234. Available from: https://doi.org/10.1104/pp.15.01907

Blondel, V.D., **Guillaume, J.-L.**, **Lambiotte, R.** & **Lefebvre, E.** (2008) Fast unfolding of communities in large networks. *Journal of Statistical Mechanics: Theory and Experiment*, **2008**(10), P10008.

Bolik, S., **Albrieux, C.**, **Schneck, E.**, **Demé, B.** & **Jouhet, J.** (2022) Sulfoquinovosyldiacylglycerol and phosphatidylglycerol bilayers share biophysical properties and are good mutual substitutes in photosynthetic membranes. *Biochimica et Biophysica Acta (BBA) - Biomembranes*, **1864**(12), 184037. Available from: https://doi.org/10.1016/J.BBAMEM.2022.184037

Boyle, N.R., **Page, M.D.**, **Liu, B.**, **Blaby, I.K.**, **Casero, D.**, **Kropat, J.** ***et al.*** (2012) Three acyltransferases and nitrogen-responsive regulator are implicated in nitrogen starvation-induced triacylglycerol accumulation in *Chlamydomonas*. *Journal of Biological Chemistry*, **287**(19), 15811–15825. Available from: https://doi.org/10.1074/JBC.M111.334052

Bray, N.L., **Pimentel, H.**, **Melsted, P.** & **Pachter, L.** (2016) Near-optimal probabilistic RNA-seq quantification. *Nature Biotechnology*, **34**(5), 525–527. Available from: https://doi.org/10.1038/NBT.3519

Breuer, G., **Evers, W.A.C.**, **de Vree, J.H.**, **Kleinegris, D.M.M.**, **Martens, D.E.**, **Wijffels, R.H.** ***et al.*** (2013) Analysis of fatty acid content and composition in microalgae. *Journal of Visualized Experiments: JoVE*, **80**, 50628. Available from: https://doi.org/10.3791/50628

Bustos, R., **Castrillo, G.**, **Linhares, F.**, **Puga, M.I.**, **Rubio, V.**, **Pérez-Pérez, J.** ***et al.*** (2010) A central regulatory system largely controls transcriptional activation and repression responses to phosphate starvation in Arabidopsis. *PLoS Genetics*, **6**(9), e1001102. Available from: https://doi.org/10.1371/journal.pgen.1001102

Cañavate, J.P., **Armada, I.** & **Hachero-Cruzado, I.** (2017) Aspects of phosphorus physiology associated with phosphate-induced polar lipid remodelling in marine microalgae. *Journal of Plant Physiology*, **214**, 28–38. Available from: https://doi.org/10.1016/J.JPLPH.2017.03.019

Canāvate, J.P., **Armada, I.**, **Riós, J.L.** & **Hachero-Cruzado, I.** (2016) Exploring occurrence and molecular diversity of betaine lipids across taxonomy of marine microalgae. *Phytochemistry*, **124**, 68–78. Available from: https://doi.org/10.1016/J.PHYTOCHEM.2016.02.007

Cánovas, F.M., **Cañas, R.A.**, **de la Torre, F.N.**, **Pascual, M.B.**, **Castro-Rodríguez, V.** & **Avila, C.** (2018) Nitrogen metabolism and biomass production in forest trees. *Frontiers in Plant Science*, **9**, 1449. Available from: https://doi.org/10.3389/FPLS.2018.01449/BIBTEX

Cernac, A. & **Benning, C.** (2004) WRINKLED1 encodes an AP2/EREB domain protein involved in the control of storage compound biosynthesis in Arabidopsis. *The Plant Journal*, **40**(4), 575–585. Available from: https://doi.org/10.1111/J.1365-313X.2004.02235.X

Chaudhry, R. & **Varacallo, M.** (2018) Biochemistry, glycolysis.

Chen, L., **Zheng, Y.**, **Dong, Z.**, **Meng, F.**, **Sun, X.**, **Fan, X.** ***et al.*** (2018) Soybean (*Glycine max*) WRINKLED1 transcription factor, GmWRI1a, positively regulates seed oil accumulation. *Molecular Genetics and Genomics*, **293**(2), 401–415. Available from: https://doi.org/10.1007/S00438-017-1393-2/FIGURES/7

Chen, M., **Tang, H.**, **Ma, H.**, **Holland, T.C.**, **Ng, K.Y.S.** & **Salley, S.O.** (2011) Effect of nutrients on growth and lipid accumulation in the green algae *Dunaliella tertiolecta*. *Bioresource Technology*, **102**(2), 1649–1655. Available from: https://doi.org/10.1016/J.BIORTECH.2010.09.062

Choi, B.Y., **Shim, D.**, **Kong, F.**, **Auroy, P.**, **Lee, Y.**, **Li-Beisson, Y.** ***et al.*** (2022) The *Chlamydomonas* transcription factor MYB1 mediates lipid accumulation under nitrogen depletion. *New Phytologist*, **235**(2), 595–610. Available from: https://doi.org/10.1111/NPH.18141

Conway, J.R., **Lex, A.** & **Gehlenborg, N.** (2017) UpSetR: an R package for the visualization of intersecting sets and their properties. *Bioinformatics (Oxford, England)*, **33**(18), 2938–2940. Available from: https://doi.org/10.1093/BIOINFORMATICS/BTX364

Csardi, G. & **Nepusz, T.** (2014) The igraph software package for complex network research. Researchgate.Net.

Del Campo, J.A., **Rodríguez, H.**, **Moreno, J.**, **Vargas, M.Á.**, **Rivas, J.** & **Guerrero, M.G.** (2003) Accumulation of astaxanthin and lutein in *Chlorella zofingiensis* (Chlorophyta). *Applied Microbiology and Biotechnology*, **64**(6), 848–854. Available from: https://doi.org/10.1007/S00253-003-1510-5

Deng, X.-D., **Gu, B.**, **Li, Y.-J.**, **Hu, X.-W.**, **Guo, J.-C.** & **Fei, X.-W.** (2012) The roles of acyl-CoA: diacylglycerol acyltransferase 2 genes in the biosynthesis of triacylglycerols by the green algae *Chlamydomonas reinhardtii*. *Molecular Plant*, **5**, 945–947. Available from: https://doi.org/10.1093/mp/sss040

Du, Z.-Y. & **Benning, C.** (2016) Triacylglycerol accumulation in photosynthetic cells in plants and algae. In: *Lipids in plant and algae development*. Cham: Springer International Publishing, pp. 179–205.

Du, Z.Y., **Lucker, B.F.**, **Zienkiewicz, K.**, **Miller, T.E.**, **Zienkiewicz, A.**, **Sears, B.B.** ***et al.*** (2018) Galactoglycerolipid lipase PGD1 is involved in thylakoid membrane remodeling in response to adverse environmental conditions in *Chlamydomonas*. *The Plant Cell*, **30**(2), 447–465. Available from: https://doi.org/10.1105/TPC.17.00446

Emms, D.M. & **Kelly, S.** (2019) OrthoFinder: phylogenetic orthology inference for comparative genomics. *Genome Biology*, **20**(1), 1–14. Available from: https://doi.org/10.1186/S13059-019-1832-Y/FIGURES/5

Fan, J., **Cui, Y.**, **Zhou, Y.**, **Wan, M.**, **Wang, W.**, **Xie, J.** ***et al.*** (2014) The effect of nutrition pattern alteration on *Chlorella pyrenoidosa* growth, lipid biosynthesis-related gene transcription. *Bioresource Technology*, **164**, 214–220. Available from: https://doi.org/10.1016/J.BIORTECH.2014.04.087

Fields, F.J., **Ostrand, J.T.** & **Mayfield, S.P.** (2018) Fed-batch mixotrophic cultivation of *Chlamydomonas reinhardtii* for high-density cultures. *Algal Research*, **33**, 109–117. Available from: https://doi.org/10.1016/J.ALGAL.2018.05.006

Fukuda, S., **Hirasawa, E.**, **Takemura, T.**, **Takahashi, S.**, **Chokshi, K.**, **Pancha, I.** ***et al.*** (2018) Accelerated triacylglycerol production without growth inhibition by overexpression of a glycerol-3-phosphate acyltransferase in the unicellular red alga *Cyanidioschyzon merolae*. *Scientific Reports*, **8**(1), 1–12. Available from: https://doi.org/10.1038/s41598-018-30809-8

Gargouri, M., **Park, J.J.**, **Holguin, F.O.**, **Kim, M.J.**, **Wang, H.**, **Deshpande, R.R.** ***et al.*** (2015) Identification of regulatory network hubs that control lipid metabolism in *Chlamydomonas reinhardtii*. *Journal of Experimental*

Botany, **66**(15), 4551–4566. Available from: https://doi.org/10.1093/jxb/erv217

Goncalves, E.C., **Koh, J.**, **Zhu, N.**, **Yoo, M.J.**, **Chen, S.**, **Matsuo, T.** ***et al.*** (2016) Nitrogen starvation-induced accumulation of triacylglycerol in the green algae: evidence for a role for ROC40, a transcription factor involved in circadian rhythm. *The Plant Journal*, **85**(6), 743–757. Available from: https://doi.org/10.1111/TPJ.13144

Gu, Z., **Eils, R.** & **Schlesner, M.** (2016) Complex heatmaps reveal patterns and correlations in multidimensional genomic data. *Bioinformatics (Oxford, England)*, **32**(18), 2847–2849. Available from: https://doi.org/10.1093/BIOINFORMATICS/BTW313

Hawrot-Paw, M., **Ratomski, P.**, **Koniuszy, A.**, **Golimowski, W.**, **Teleszko, M.** & **Grygier, A.** (2021) Fatty acid profile of microalgal oils as a criterion for selection of the best feedstock for biodiesel production. *Energies*, **14**(21), 7334. Available from: https://doi.org/10.3390/EN14217334

He, M., **Qin, C.-X.**, **Wang, X.** & **Ding, N.-Z.** (2020) Plant unsaturated fatty acids: biosynthesis and regulation. *Frontiers in Plant Science*, **11**, 390.

Hovde, B.T., **Hanschen, E.R.**, **Steadman, C.R.**, **Lo, C.**, **Kunde, Y.**, **Davenport, K.** ***et al.*** (2018) Genomic characterization reveals significant divergence within *Chlorella*. *Algal Research*, **35**, 449–461. Available from: https://doi.org/10.1016/j.algal.2018.09.012

Hu, Q., **Sommerfeld, M.**, **Jarvis, E.**, **Ghirardi, M.**, **Posewitz, M.**, **Seibert, M.** ***et al.*** (2008) Microalgal triacylglycerols as feedstocks for biofuel production: perspectives and advances. *Plant Journal*, **54**(4), 621–639. Available from: https://doi.org/10.1111/j.1365-313X.2008.03492.x

Huang, B., **Marchand, J.**, **Thiriet-Rupert, S.**, **Carrier, G.**, **Saint-Jean, B.**, **Lukomska, E.** ***et al.*** (2019) Betaine lipid and neutral lipid production under nitrogen or phosphorus limitation in the marine microalga *Tisochrysis lutea* (Haptophyta). *Algal Research*, **40**, 101506. Available from: https://doi.org/10.1016/J.ALGAL.2019.101506

Illman, A.M., **Scragg, A.H.** & **Shales, S.W.** (2000) Increase in *Chlorella* strains calorific values when grown in low nitrogen medium. *Enzyme and Microbial Technology*, **27**(8), 631–635. Available from: https://doi.org/10.1016/S0141-0229(00)00266-0

Ischebeck, T., **Krawczyk, H.E.**, **Mullen, R.T.**, **Dyer, J.M.** & **Chapman, K.D.** (2020) Lipid droplets in plants and algae: distribution, formation, turnover and function. *Seminars in Cell & Developmental Biology*, **108**, 82–93. Available from: https://doi.org/10.1016/J.SEMCDB.2020.02.014

Jin, J., **Tian, F.**, **Yang, D.C.**, **Meng, Y.Q.**, **Kong, L.**, **Luo, J.** ***et al.*** (2017) PlantTFDB 4.0: toward a central hub for transcription factors and regulatory interactions in plants. *Nucleic Acids Research*, **45**(D1), D1040–D1045. Available from: https://doi.org/10.1093/NAR/GKW982

Kamalanathan, M., **Gleadow, R.** & **Beardall, J.** (2015) Impacts of phosphorus availability on lipid production by *Chlamydomonas reinhardtii*. *Algal Research*, **12**, 191–196. Available from: https://doi.org/10.1016/J.ALGAL.2015.08.021

Kobayashi, K. (2016) Role of membrane glycerolipids in photosynthesis, thylakoid biogenesis and chloroplast development. *Journal of Plant Research*, **129**(4), 565–580. Available from: https://doi.org/10.1007/S10265-016-0827-Y

Kolde, R., **Laur, S.**, **Adler, P.** & **Vilo, J.** (2012) Robust rank aggregation for gene list integration and meta-analysis. *Bioinformatics*, **28**(4), 573–580. Available from: https://doi.org/10.1093/BIOINFORMATICS/BTR709

Kong, F., **Romero, I.T.**, **Warakanont, J.** & **Li-Beisson, Y.** (2018) Lipid catabolism in microalgae. *New Phytologist*, **218**(4), 1340–1348. Available from: https://doi.org/10.1111/NPH.15047

Kumar Sharma, A., **Mühlroth, A.**, **Jouhet, J.**, **Maréchal, E.**, **Alipanah, L.**, **Kissen, R.** ***et al.*** (2020) The Myb-like transcription factor phosphorus starvation response (PtPSR) controls conditional P acquisition and remodelling in marine microalgae. *New Phytologist*, **225**(6), 2380–2395. Available from: https://doi.org/10.1111/NPH.16248

La Russa, M., **C, B.**, **A, U.**, **A, D.**, **E, F.**, **O, K.** ***et al.*** (2012) Functional analysis of three type-2 DGAT homologue genes for triacylglycerol production in the green microalga *Chlamydomonas reinhardtii*. *Journal of Biotechnology*, **162**(1), 13–20. Available from: https://doi.org/10.1016/J.JBIOTEC.2012.04.006

Lammers, P.J., **Huesemann, M.**, **Boeing, W.**, **Anderson, D.B.**, **Arnold, R.G.**, **Bai, X.** ***et al.*** (2017) Review of the cultivation program within the National Alliance for Advanced Biofuels and Bioproducts. *Algal Research*, **22**, 166–186. Available from: https://doi.org/10.1016/J.ALGAL.2016.11.021

Levasseur, W., **Perré, P.** & **Pozzobon, V.** (2020) A review of high value-added molecules production by microalgae in light of the classification. *Biotechnology Advances*, **41**, 107545. Available from: https://doi.org/10.1016/J.BIOTECHADV.2020.107545

Liang, Y., **Sarkany, N.** & **Cui, Y.** (2009) Biomass and lipid productivities of *Chlorella vulgaris* under autotrophic, heterotrophic and mixotrophic growth conditions. *Biotechnology Letters*, **31**(7), 1043–1049. Available from: https://doi.org/10.1007/S10529-009-9975-7

Linlin, Y. (2023) ggvenn: draw Venn diagram by "ggplot2" (R package version 0.1.10).

Love, M.I., **Huber, W.** & **Anders, S.** (2014) Moderated estimation of fold change and dispersion for RNA-seq data with DESeq2. *Genome Biology*, **15**(12), 550. Available from: https://doi.org/10.1186/S13059-014-0550-8

Maltsev, Y., **Kulikovskiy, M.** & **Maltseva, S.** (2023) Nitrogen and phosphorus stress as a tool to induce lipid production in microalgae. *Microbial Cell Factories*, **22**(1), 1–22. Available from: https://doi.org/10.1186/S12934-023-02244-6

Margolin, A.A., **Nemenman, I.**, **Basso, K.**, **Wiggins, C.**, **Stolovitzky, G.**, **Favera, R.D.** ***et al.*** (2006) ARACNE: an algorithm for the reconstruction of gene regulatory networks in a mammalian cellular context. *BMC Bioinformatics*, **7**(1), S7. Available from: https://doi.org/10.1186/1471-2105-7-S1-S7

Margolin, A.A., **Wang, K.**, **Lim, W.K.**, **Kustagi, M.**, **Nemenman, I.** & **Califano, A.** (2006) Reverse engineering cellular networks. *Nature Protocols*, **1**(2), 662–671. Available from: https://doi.org/10.1038/nprot.2006.106

Mathiot, C., **Ponge, P.**, **Gallard, B.**, **Sassi, J.F.**, **Delrue, F.** & **Le Moigne, N.** (2019) Microalgae starch-based bioplastics: screening of ten strains and plasticization of unfractionated microalgae by extrusion. *Carbohydrate Polymers*, **208**, 142–151. Available from: https://doi.org/10.1016/J.CARBPOL.2018.12.057

Meï, C., **Michaud, M.**, **Cussac, M.**, **Albrieux, C.**, **Gros, V.**, **Maréchal, E.** ***et al.*** (2015) Levels of polyunsaturated fatty acids correlate with growth rate in plant cell cultures. *Scientific Reports*, **5**(1), 15207. Available from: https://doi.org/10.1038/SREP15207

Mimouni, V., **Couzinet-Mossion, A.**, **Ulmann, L.** & **Wielgosz-Collin, G.** (2018) Lipids from microalgae. In: Levine, I.A. & Fleurence, J. (Eds.) *Microalgae in health and disease prevention*. London, England: Elsevier (Academic Press), pp. 109–131. Available from: https://doi.org/10.1016/B978-0-12-811405-6.00005-0

Moudříková, Š., **Sadowsky, A.**, **Metzger, S.**, **Nedbal, L.**, **Mettler-Altmann, T.** & **Mojzeš, P.** (2017) Quantification of polyphosphate in microalgae by Raman microscopy and by a reference enzymatic assay. *Analytical Chemistry*, **89**(22), 12006–12013. Available from: https://doi.org/10.1021/ACS.ANALCHEM.7B02393/ASSET/IMAGES/LARGE/AC-2017-02393D_0004.JPEG

Mühlroth, A., **Winge, P.**, **El Assimi, A.**, **Jouhet, J.**, **Maréchal, E.**, **Hohmann-Marriott, M.F.** ***et al.*** (2017) Mechanisms of phosphorus acquisition and lipid class remodeling under P limitation in a marine microalga. *Plant Physiology*, **175**(4), 1543–1559. Available from: https://doi.org/10.1104/PP.17.00621

Mulgund, A. (2022) Increasing lipid accumulation in microalgae through environmental manipulation, metabolic and genetic engineering: a review in the energy NEXUS framework. *Energy Nexus*, **5**, 100054. Available from: https://doi.org/10.1016/J.NEXUS.2022.100054

Neofotis, P., **Huang, A.**, **Sury, K.**, **Chang, W.**, **Joseph, F.**, **Gabr, A.** ***et al.*** (2016) Characterization and classification of highly productive microalgae strains discovered for biofuel and bioproduct generation. *Algal Research*, **15**, 164–178. Available from: https://doi.org/10.1016/J.ALGAL.2016.01.007

Oishi, Y., **Otaki, R.**, **Iijima, Y.**, **Kumagai, E.**, **Aoki, M.**, **Tsuzuki, M.** ***et al.*** (2022) Diacylglyceryl-N,N,N-trimethylhomoserine-dependent lipid remodeling in a green alga, *Chlorella kessleri*. *Communications Biology*, **5**(1), 19. Available from: https://doi.org/10.1038/s42003-021-02927-z

Paysan-Lafosse, T., **Blum, M.**, **Chuguransky, S.**, **Grego, T.**, **Pinto, B.L.**, **Salazar, G.A.** ***et al.*** (2023) InterPro in 2022. *Nucleic Acids Research*, **51**(D1), D418–D427. Available from: https://doi.org/10.1093/NAR/GKAC993

Pelah, D., **Sintov, A.** & **Cohen, E.** (2004) The effect of salt stress on the production of canthaxanthin and astaxanthin by *Chlorella zofingiensis* grown under limited light intensity. *World Journal of Microbiology and Biotechnology*, **20**(5), 483–486. Available from: https://doi.org/10.1023/B:WIBI.0000040398.93103.21

Peng, K.T., **Zheng, C.N.**, **Xue, J.**, **Chen, X.Y.**, **Yang, W.D.**, **Liu, J.S.** ***et al.*** (2014) Delta 5 fatty acid desaturase upregulates the synthesis of

polyunsaturated fatty acids in the marine diatom *Phaeodactylum tricornutum*. *Journal of Agricultural and Food Chemistry*, **62**(35), 8773–8776. Available from: https://doi.org/10.1021/JF5031086

Radakovits, R., **Eduafo, P.M.** & **Posewitz, M.C.** (2011) Genetic engineering of fatty acid chain length in *Phaeodactylum tricornutum*. *Metabolic Engineering*, **13**(1), 89–95. Available from: https://doi.org/10.1016/J.YMBEN.2010.10.003

Riekhof, W.R., **Sears, B.B.** & **Benning, C.** (2005) Annotation of genes involved in glycerolipid biosynthesis in *Chlamydomonas reinhardtii*: discovery of the betaine lipid synthase BTA1Cr. *Eukaryotic Cell*, **4**(2), 242–252. Available from: https://doi.org/10.1128/EC.4.2.242-252.2005/ASSET/3535DA16-60FA-46BC-A97F-4E6C0E4771F4/ASSETS/GRAPHIC/ZEK0020523910007.JPEG

Ritchie, R.J., **Sma-Air, S.** & **Phongphattarawat, S.** (2021) Using DMSO for chlorophyll spectroscopy. *Journal of Applied Phycology*, **33**(4), 2047–2055. Available from: https://doi.org/10.1007/S10811-021-02438-8/FIGURES/4

Robinson, M.D., **McCarthy, D.J.** & **Smyth, G.K.** (2010) edgeR: a bioconductor package for differential expression analysis of digital gene expression data. *Bioinformatics*, **26**(1), 139–140. Available from: https://doi.org/10.1093/BIOINFORMATICS/BTP616

Romero-Campero, F.J., **Perez-Hurtado, I.**, **Lucas-Reina, E.**, **Romero, J.M.** & **Valverde, F.** (2016) ChlamyNET: a *Chlamydomonas* gene co-expression network reveals global properties of the transcriptome and the early setup of key co-expression patterns in the green lineage. *BMC Genomics*, **17**(1), 227. Available from: https://doi.org/10.1186/S12864-016-2564-Y

Sajjadi, B., **Chen, W.Y.**, **Raman, A.A.A.** & **Ibrahim, S.** (2018) Microalgae lipid and biomass for biofuel production: a comprehensive review on lipid enhancement strategies and their effects on fatty acid composition. *Renewable and Sustainable Energy Reviews*, **97**, 200–232. Available from: https://doi.org/10.1016/j.rser.2018.07.050

Sasaki, Y. & **Nagano, Y.** (2004) Plant acetyl-CoA carboxylase: structure, biosynthesis, regulation, and gene manipulation for plant breeding. *Bioscience, Biotechnology, and Biochemistry*, **68**(6), 1175–1184. Available from: https://doi.org/10.1271/BBB.68.1175

Schläpfer, P., **Zhang, P.**, **Wang, C.**, **Kim, T.**, **Banf, M.**, **Chae, L.** ***et al.*** (2017) Genome-wide prediction of metabolic enzymes, pathways, and gene clusters in plants. *Plant Physiology*, **173**(4), 2041–2059. Available from: https://doi.org/10.1104/PP.16.01942

Schmollinger, S., **Mühlhaus, T.**, **Boyle, N.R.**, **Blaby, I.K.**, **Casero, D.**, **Mettler, T.** ***et al.*** (2014) Nitrogen-sparing mechanisms in *Chlamydomonas* affect the transcriptome, the proteome, and photosynthetic metabolism. *The Plant Cell*, **26**(4), 1410–1435. Available from: https://doi.org/10.1105/TPC.113.122523

Sharma, S., **Joshi, J.**, **Kataria, S.**, **Verma, S.K.**, **Chatterjee, S.**, **Jain, M.** ***et al.*** (2020) Regulation of the Calvin cycle under abiotic stresses: an overview. In: *Plant life under changing environment*. Cambridge, MA, USA: Elsevier (Academic Press), pp. 681–717.

Shi, X.-M. & **Chen, F.** (2002) High-yield production of lutein by the green microalga *Chlorella protothecoidesin* heterotrophic fed-batch culture. *Biotechnology Progress*, **18**(4), 723–727. Available from: https://doi.org/10.1021/BP0101987

Soneson, C., **Love, M.I.** & **Robinson, M.D.** (2015) Differential analyses for RNA-seq: transcript-level estimates improve gene-level inferences. *F1000Research*, **4**, 1521. Available from: https://doi.org/10.12688/F1000RESEARCH.7563.2

Song, X., **Liu, B.F.**, **Kong, F.**, **Ren, N.Q.** & **Ren, H.Y.** (2022) Overview on stress-induced strategies for enhanced microalgae lipid production: application, mechanisms and challenges. *Resources, Conservation and Recycling*, **183**, 106355. Available from: https://doi.org/10.1016/J.RESCONREC.2022.106355

Südfeld, C., **Hubáček, M.**, **Figueiredo, D.**, **Naduthodi, I.S.**, **Van Der Oost, J.**, **Wijffels, R.H.** ***et al.*** (2021) High-throughput insertional mutagenesis reveals novel targets for enhancing lipid accumulation in *Nannochloropsis oceanica*. *Metabolic Engineering*, **66**, 1096–7176. Available from: https://doi.org/10.1016/j.ymben.2021.04.012

Sun, X.M., **Ren, L.J.**, **Zhao, Q.Y.**, **Ji, X.J.** & **Huang, H.** (2019) Enhancement of lipid accumulation in microalgae by metabolic engineering. *Biochimica et Biophysica Acta (BBA) – Molecular and Cell Biology of Lipids*, **1864**(4), 552–566. Available from: https://doi.org/10.1016/J.BBALIP.2018.10.004

Theodoulou, F.L. & **Eastmond, P.J.** (2012) Seed storage oil catabolism: a story of give and take. *Current Opinion in Plant Biology*, **15**(3), 322–328.

Tian, F., **Yang, D.C.**, **Meng, Y.Q.**, **Jin, J.** & **Gao, G.** (2020) PlantRegMap: charting functional regulatory maps in plants. *Nucleic Acids Research*, **48** (D1), D1104–D1113. Available from: https://doi.org/10.1093/NAR/GKZ1020

Trentacoste, E.M., **Shrestha, R.P.**, **Smith, S.R.**, **Glé, C.**, **Hartmann, A.C.**, **Hildebrand, M.** ***et al.*** (2013) Metabolic engineering of lipid catabolism increases microalgal lipid accumulation without compromising growth. *Proceedings of the National Academy of Sciences of the United States of America*, **110**(49), 19748–19753. Available from: https://doi.org/10.1073/PNAS.1309299110

Tsai, C.H., **Warakanontb, J.**, **Takeuchic, T.**, **Sears, B.B.**, **Moellering, E.R.** & **Benningc, C.** (2014) The protein compromised hydrolysis of triacylglycerols 7 (CHT7) acts as a repressor of cellular quiescence in *Chlamydomonas*. *Proceedings of the National Academy of Sciences of the United States of America*, **111**(44), 15833–15838. Available from: https://doi.org/10.1073/PNAS.1414567111/SUPPL_FILE/PNAS.1414567111.SD03.XLSX

Tsai, C.H., **Zienkiewicz, K.**, **Amstutz, C.L.**, **Brink, B.G.**, **Warakanont, J.**, **Roston, R.** ***et al.*** (2015) Dynamics of protein and polar lipid recruitment during lipid droplet assembly in *Chlamydomonas reinhardtii*. *The Plant Journal*, **83**(4), 650–660. Available from: https://doi.org/10.1111/TPJ.12917

Vijayan, J., **Wase, N.**, **Liu, K.**, **Morse, W.**, **Zhang, C.** & **Riekhof, W.R.** (2024) ROS-mediated thylakoid membrane remodeling and triacylglycerol biosynthesis under nitrogen starvation in the alga *Chlorella sorokiniana*. *Frontiers in Plant Science*, **15**, 1418049. Available from: https://doi.org/10.3389/FPLS.2024.1418049/BIBTEX

Wan, M., **Liu, P.**, **Xia, J.**, **Rosenberg, J.N.**, **Oyler, G.A.**, **Betenbaugh, M.J.** ***et al.*** (2011) The effect of mixotrophy on microalgal growth, lipid content, and expression levels of three pathway genes in *Chlorella sorokiniana*. *Applied Microbiology and Biotechnology*, **91**(3), 835–844. Available from: https://doi.org/10.1007/S00253-011-3399-8

Wang, X., **Wei, H.**, **Mao, X.** & **Liu, J.** (2019) Proteomics analysis of lipid droplets from the oleaginous alga *Chromochloris zofingiensis* reveals novel proteins for lipid metabolism. *Genomics, Proteomics & Bioinformatics*, **17**(3), 260–272. Available from: https://doi.org/10.1016/J.GPB.2019.01.003

Wang, Y. & **Chen, T.** (2008) The biosynthetic pathway of carotenoids in the astaxanthin-producing green alga *Chlorella zofingiensis*. *World Journal of Microbiology and Biotechnology*, **24**(12), 2927–2932. Available from: https://doi.org/10.1007/S11274-008-9834-Z

Wang, Z., **Kuo, H.F.** & **Chiou, T.J.** (2021) Intracellular phosphate sensing and regulation of phosphate transport systems in plants. *Plant Physiology*, **187** (4), 2043–2055. Available from: https://doi.org/10.1093/PLPHYS/KIAB343

Wickham, H. (2016) *ggplot2: elegant graphics for data analysis*. New York: Springer-Verlag. Available from: https://ggplot2.tidyverse.org

Winter, G., **Todd, C.D.**, **Trovato, M.**, **Forlani, G.** & **Funck, D.** (2015) Physiological implications of arginine metabolism in plants. *Frontiers in Plant Science*, **6**, 534. Available from: https://doi.org/10.3389/FPLS.2015.00534

Xing, G., **Li, J.**, **Li, W.**, **Lam, S.M.**, **Yuan, H.**, **Shui, G.** ***et al.*** (2021) AP2/ERF and R2R3-MYB family transcription factors: potential associations between temperature stress and lipid metabolism in *Auxenochlorella protothecoides*. *Biotechnology for Biofuels*, **14**(1), 1–16. Available from: https://doi.org/10.1186/S13068-021-01881-6/FIGURES/8

Xue, J., **Niu, Y.F.**, **Huang, T.**, **Yang, W.D.**, **Liu, J.S.** & **Li, H.Y.** (2015) Genetic improvement of the microalga *Phaeodactylum tricornutum* for boosting neutral lipid accumulation. *Metabolic Engineering*, **27**, 1–9. Available from: https://doi.org/10.1016/J.YMBEN.2014.10.002

Yaakob, M.A., **Mohamed, R.M.S.R.**, **Al-Gheethi, A.**, **Gokare, R.A.** & **Ambati, R.R.** (2021) Influence of nitrogen and phosphorus on microalgal growth, biomass, lipid, and fatty acid production: an overview. *Cells*, **10**(2), 393. Available from: https://doi.org/10.3390/CELLS10020393

Yu, L., **Zhou, C.**, **Fan, J.**, **Shanklin, J.** & **Xu, C.** (2021) Mechanisms and functions of membrane lipid remodeling in plants. *The Plant Journal*, **107**(1), 37–53. Available from: https://doi.org/10.1111/TPJ.15273

Zäuner, S., **Jochum, W.**, **Bigorowski, T.** & **Benning, C.** (2012) A cytochrome b5-containing plastid-located fatty acid desaturase from *Chlamydomonas reinhardtii*. *Eukaryotic Cell*, **11**(7), 856–863. Available from: https://doi.org/10.1128/EC.00079-12

Zhang, Y. & **Fernie, A.R.** (2023) The role of TCA cycle enzymes in plants. *Advanced Biology*, **7**, 2200238.

Zhu, S., **Wang, Y.**, **Xu, J.**, **Shang, C.**, **Wang, Z.**, **Xu, J.** ***et al.*** (2015) Luxury uptake of phosphorus changes the accumulation of starch and lipid in *Chlorella* sp. under nitrogen depletion. *Bioresource Technology*, **198**, 165–171. Available from: https://doi.org/10.1016/J.BIORTECH.2015.08.142